MDA5 multimerization on LINE RNA drives pathogenic extracellular immune complexes in autoimmunity

Tiffany Hsu[1,2,3], Xi Wang[1,2], Yukari Isayama[4], Viktoria Jung[5], Jiayan Zhang[4], Eveline van Gompel[6,7,8], Hadil Maadadi[5], Celia Torres[1,2], Akiko Shimazaki-Takahashi[4], Nina Kurihara[4], Mariko Kondo[9], Marina Galesic[6,7,8], Antonella Notarnicola[6,7,8], Sharmin Sultana[10], Athony Maeda[10], Ruth Ann Vleugels[11], Paul Dellaripa[3], Takashi Yamashita[12], Yukiko Ito[12], Kentaro Awaji[12], Hirohito Kotani[12], Kazuki M. Matsuda[12], Begum Horuluogu[6,7,8], Caroline Grönwall[6,7,8], Vijay Joshua[6,7,8], Yoshinori Ukai[9], Naoki Hosomi[9], Denisa D. Wagner[5,13,14], Ingrid E. Lundberg[6,7,8]*, Kazuki Kato[4]*, Sun Hur[1,2]*

[1]Howard Hughes Medical Institute and Program in Cellular and Molecular Medicine, Boston Children's Hospital, MA 02115, USA
[2]Department of Biological Chemistry and Molecular Pharmacology, Harvard Medical School,
Boston, MA 02115, USA
[3]Division of Rheumatology, Inflammation, and Immunity, Brigham and Women's Hospital, Harvard Medical School, Boston, MA 02115, USA
[4]Mechanistic Immunology Research Unit, Institute of Integrated Research, Institute of Science Tokyo 113-8510, Japan
[5]Program in Cellular and Molecular Medicine, Boston Children's Hospital, MA 02115, USA
[6]Division of Rheumatology, Department of Medicine, Solna, Karolinska Institutet, Stockholm, Sweden
[7]Division of Gastroenterology, Dermatology and Rheumatology, Theme Inflammation and Aging, Karolinska University Hospital, Stockholm, Sweden
[8]Center for Molecular Medicine, Karolinska University Hospital, Stockholm, Sweden
[9]Perseus Proteomics Inc., Tokyo , Japan
[10]Division of Pulmonary and Critical Care Medicine, Brigham and Women's Hospital, Boston, MA 02115, USA
[11]Department of Dermatology, Brigham and Women's Hospital, Harvard Medical School, Boston, MA 02115, USA
[12]Department of Dermatology, University of Tokyo Graduate School of Medicine, Tokyo, Japan
[13]Department of Pediatrics, Harvard Medical School, 25 Shattuck Street, Boston, MA 02115, USA;
[14]Division of Hematology/Oncology, Boston Children's Hospital, 1 Blackfan Circle, Boston, MA 02115, USA;

*co-correspondence

Abstract

Autoantibodies are hallmarks of many autoimmune diseases, but their potential pathogenic roles, particularly for those targeting intracellular proteins, remain unclear. Anti-MDA5-positive dermatomyositis (anti-MDA5 DM) is characterized by autoantibodies against the intracellular protein MDA5[1,2], a conserved innate immune receptor that recognizes viral dsRNA by forming filaments[3]. Here, using four patient-derived monoclonal autoantibodies (mAbs), we reconstitute and define the molecular architecture, biogenesis, and immunological activity of pathogenic MDA5 immune complexes. Our cryo-EM analysis revealed that these mAbs bind dsRNA-scaffolded MDA5 filaments in at least two distinct binding modes, each exhibiting striking epitope convergence. Extracellular immune complexes formed between mAbs and filamentous, but not monomeric, MDA5 potently activate multiple innate immune pathways, with the magnitude of activation determined by antibody binding mode and immune-complex stoichiometry. Antibody bivalency further crosslinks MDA5 filaments into higher-order aggregates with heightened immunostimulatory activity, demonstrating an active role of autoantibodies in shaping immune complex architecture. Analysis of patient plasma reveals elevated levels of extracellular MDA5 filaments and identifies LINE retroelement-derived dsRNA as a structural scaffold. Notably, MDA5 immune complexes induce endogenous LINE dsRNA expression, likely promoting additional MDA5 filament formation and extracellular release through inflammatory cell death. These data thus support a self-amplifying inflammatory cycle as a pathogenic mechanism for anti-MDA5 DM. Collectively, our study defines a broadly applicable architectural principle, in which higher-order organization and binding modes of autoantibodies—beyond antibody affinity or nucleic acid presence alone—govern innate immune activation.

Main text

Anti-MDA5 DM is a multisystem inflammatory disease associated with significant morbidity and mortality[4-6]. Diagnosis relies upon the presence of IgG anti-MDA5 autoantibodies and a distinctive constellation of symptoms. Patients typically present with rashes, an unusual predisposition to ulceration, and interstitial lung disease that can rapidly progress (RP-ILD) to respiratory failure[4-6]. In patients with RP-ILD, therapeutic options are limited, and disease courses are often fulminant and fatal[6,7]. At the molecular level, anti-MDA5 DM patients display strong features of systemic type I interferon (IFN) signaling, and evidence of broad dysregulation across both innate and adaptive immune cells[8-10]. Accumulating evidence suggests that anti-MDA5 antibodies contribute to disease pathogenesis[11-13], yet the underlying mechanisms—and the precise molecular nature of the immune-stimulatory entity, including whether the antibody alone is sufficient—remain debated. Thus, anti-MDA5 DM provides an important framework for investigating how autoantibodies targeting intracellular proteins can drive immune-mediated disease.

The target antigen MDA5 belongs to the RIG-I–like receptor (RLR) family and recognizes long stretches of dsRNA that accumulate during viral replication[14]. Several viruses, including coronaviruses and picornaviruses, generate long dsRNA replication intermediates that can activate MDA5[14]. Under pathological conditions, however, shorter but abundant cellular dsRNAs, such as ~300 bp hairpin structures formed by inverted-repeat Alu transcripts, have also been shown to activate MDA5[15-17]. This length-selective detection is mediated by MDA5 filament formation along dsRNA[18-20]. In the resting state, MDA5 is monomeric; upon engaging dsRNA, it assembles into helical filaments that recruit the dimeric E3 ligase TRIM65 via a bivalent binding mode[21]. TRIM65 then catalyzes K63-linked ubiquitination of MDA5, inducing formation of signaling-competent state of MDA5 that activates the adaptor MAVS[20]. MAVS then forms a signaling scaffold on the mitochondrial surface, activating IRF3 and NF-κB for induction of type I IFNs and pro-inflammatory cytokines[22]. While these intracellular signaling functions of MDA5 are well characterized, both in antiviral immunity and in monogenic interferonopathies[14,23], whether MDA5 has any extracellular function has been unclear.

Here, we report an integrated biochemical, structural, and functional characterization of four monoclonal antibodies (mAbs) derived from anti-MDA5 DM patients and present evidence directly linking autoantibodies in complex with extracellular MDA5 filaments to disease pathogenesis in anti-MDA5 DM.

Patient-derived mAbs bind MDA5 filaments in two distinct modes and can aggregate filaments.

To investigate disease pathogenesis, we analyzed B cells isolated from anti-MDA5 DM patients. Single antibody-secreting cells (ASCs) were loaded onto individual wells, and culture supernatants were screened for MDA5 reactivity, followed by cloning of antigen-specific antibodies (Extended Data Figure 1a). This approach led to the identification of two distinct MDA5-specific monoclonal antibodies (mAbs), NP6 and NP8, from one Japanese patient (Extended Data Table 1). Neither mAb bound RIG-I or LGP2, other members of RLR family with homologous helicase domain (Extended Data Figure 1b). Both antibodies were IgG1 isotype and utilized VH3 family-encoded heavy chains (IgHV3-74 for NP6 and IgHV3-73 for NP8) paired with lambda light chains (IgLV3-1 and IgLV1-47, respectively, Extended Data Figure 1c). Importantly, in the study we also included two additional anti-MDA5 mAbs (F01 and F12) that were previously generated from a Swedish patient by sorting antigen-specific B cells using MDA5 antigen probes[24]. F01 utilizes IgHV3-7 and IgLV3-1, whereas F12 utilizes IgHV3-73 and IgLV1-47[24]. Strikingly, NP6 was found to share light chain gene usage with F01 (hereafter class I, Figure 1a) and NP8 shares identical heavy and light chain gene usage with F12 (class II).

To characterize how these mAbs recognize MDA5, we performed sandwich ELISA assays in which antibodies were immobilized, titrated with FLAG-tagged MDA5, followed by detection with anti-FLAG antibody. Because MDA5 exists as a monomer in its resting state and forms filaments upon binding dsRNA, both antigenic states were examined. NP6 and F01 (class I mAbs) bound monomeric MDA5 and MDA5 filaments assembled on in vitro transcribed 512 bp dsRNA with comparable apparent affinity (NP6 K_d = 0.9 vs. 1.3 nM; F01 K_d = 1.2 vs. 1.6 nM, Figure 1b). In contrast, NP8 and F12 (class II mAbs) showed a strong preference for filamentous MDA5, binding the filament ~35-fold more tightly than the monomeric form (NP8 K_d = 73.9 vs. 2.1 nM; F12 K_d = 85.1 vs. 2.4 nM, Figure 1b).

To define the structural basis for this differential specificity, we determined cryo-EM structures of MDA5 filaments on dsRNA in complex with Fab fragments of F01 and F12 and single-chain variable fragments (scFvs) of NP6 and NP8 (Extended Data Table 2). MDA5 construct lacking the N-terminal CARD signaling domains (MDA5ΔN) with the gain-of-function mutation G495R that increases filament stability[25] was used (Figure 1c). MDA5 filaments bound by mAbs were computationally segmented into 3-5 MDA5 protomers and analyzed by single-particle or helical reconstruction (Figure 1c, see Methods). Structures of MDA5 bound to the class I mAbs NP6 and F01 were well resolved, enabling accurate model building (Extended Data Figures 2 and 3). Both antibodies recognized an identical epitope on the Hel2i domain of MDA5 (residues 670–690) and bound in nearly identical orientations, despite their divergent heavy chain usage and CDR3 sequences (Figure 1d, Extended Data Figure 1d, 4a).

Mutational analysis identified Lys685 in MDA5 as the most critical residue for binding both NP6 and F1, although other residues also contributed (Extended Data Figure 4b). Notably, with both antibodies, Lys685 is coordinated by germline-encoded residues within the IgLV3-1 light chain (Tyr32 in CDR1, Asp51 in CDR2, and Asn66 in the framework, Figure 1e), which is shared between NP6 and F1. Similar germline-encoded lysine recognition by IgLV3-1 has been reported across multiple antibodies targeting viral epitopes[26] (Extended Data Figure 4c), suggesting that intrinsic germline specificity contributes to epitope convergence in class I antibodies. Further supporting the importance of the germline-encoded residues, none of the somatically mutated residues directly contact MDA5 (Extended Data Figure 1e).

Cryo-EM reconstructions of MDA5 filaments bound to class II mAbs NP8 and F12 displayed lower local resolution for the mAbs, precluding high-confidence atomic model building. We therefore docked AlphaFold-predicted antibody models together with known MDA5 structure (PDB ID 7JL0)[21] into the density (Extended Data Figures 5 and 6). Unlike class I mAbs, which bind an individual MDA5 protomer, class II mAbs appeared to contact two adjacent protomers within the filament (Figure 1f), explaining their preference for filaments. One interaction, associated with stronger density, involves the MDA5 C-terminal domain (CTD), whereas the second interaction involves Hel2i of the neighboring protomer, near a likely disordered loop (residue 645-662) that is absent from previous MDA5 structures[20,21,27] (Figure 1f). Interestingly, deletion of the Hel2i loop abolished both NP8 and F12 binding to monomeric MDA5, whereas CTD deletion had minimal impact (Extended Data Figure 4b), indicating that Hel2i provides the primary binding interface. The intrinsically disordered nature of this Hel2i loop likely resulted in positional heterogeneity of class II mAbs, accounting for their weaker density and lower local resolution. Nonetheless, the shared dependence of NP8 and F12 on the Hel2i loop indicates epitope convergence between the two class II mAbs derived from the two independent patients, analogous to that observed for class I mAbs.

Having determined the structures of antibody variable fragments bound to MDA5 filaments, we next asked how intact IgGs engage MDA5 filaments. The structures suggest that the two Fab arms within a single IgG cannot simultaneously bind the same MDA5 filament, but instead could interact with two separate filaments, predicting antibody-mediated filament bridging and aggregation (Figure 1g). Consistent with this model, addition of NP6 mAbs induced extensive filament cross-bridging and aggregations, yielding structures that can reach several microns in size, with no observable individual non-bridged filaments (Figure 1h). In contrast, no such aggregation was observed when NP6 was incubated with monomeric MDA5 (Extended Data Figure 4d). Similar filament aggregation was also observed with NP8 mAbs; however, individual filaments were also visible (Extended Data Figure 4d), indicating less efficient cross-bridging. This difference was independently confirmed by an orthogonal pull-down assay (Figure 1i), in which Strep-tagged MDA5 filament formed on 112 bp dsRNA efficiently co-purified non-tagged MDA5 filament on 162 bp dsRNA in the presence of NP6, but much less so with NP8. Similarly, both F01 and F12 induced filament aggregation, with F01 more effectively depleting individual filaments (Extended Data Figure 4d). Consistent with the importance of bivalency, Fab fragments of F01 and F12 did not induce filament aggregation. One possible explanation for the superior filament-bridging activity of class I Abs is that their binding mode positions one Fab arm on the MDA5 filament in a manner that leaves the second Fab arm more accessible for binding another filament.

Collectively, these results indicate that all four mAbs recognize MDA5 filaments with high affinity but differ in binding mode. Class I antibodies (NP6 and F1) bind both monomeric and filamentous MDA5 and efficiently crosslink filaments, whereas class II antibodies (NP8 and F12) preferentially recognize filamentous MDA5 and exhibit reduced interfilament-bridging activity. Notably, in both class I and II, Abs from two unrelated patients converge on shared epitopes, with class I Abs clearly showing epitope recognition by germline-encoded residues, suggesting an intrinsic predisposition of MDA5 to function as an autoantigen.

MDA5 filament immune complex activates type I interferon signaling in a binding mode-dependent manner.

We next examined whether patient-derived anti-MDA5 mAbs can activate immune responses, and whether such activity requires immune complex (IC) formation with monomeric vs. filamentous MDA5. THP-1-derived macrophages were used as a model system. Using purified recombinant mAbs, MDA5ΔN and in vitro transcribed 512 bp dsRNA, we formed complexes in various combinations and stimulated THP-1 macrophages for 4 hours. Of note, all IC stimulations were performed without the use of transfection reagents or other intracellular delivery systems.

RNA-seq analysis showed that THP-1 cells incubated with NP6 mAb + dsRNA, NP6 + monomeric MDA5, or isotype control antibody + MDA5 filament formed on dsRNA showed minimal immune signaling, compared to the mock control (Extended Data Figure 7a, Supplementary Table 1). In contrast, NP6 + filamentous MDA5 (filament ICs) induced strong induction of immune-related genes, most prominently type I and II IFN signatures characteristic of anti-MDA5 DM[8-10] (Figure 2a, 2b). Interferon-stimulated genes such as *IFIH1* (encoding MDA5), *IFIT3*, *CXCL10*, and *MX2* were also induced (see Supplementary Table 1 for the full gene list). NP8 mAb also showed filament IC-specific immune response (Figure 2b, Extended Data Figure 7b, 7c), which was seen with F01 and F12 mAbs as well (Figure 2c). Consistent with the importance of the filamentous state of MDA5 for antiviral innate immune activation, the gain-of-function mutation G495R that stabilizes filaments[25] increased IFN-β induction (Extended Data Figure 7d). IFN-β ELISA further confirmed filament-specific THP-1 activation for both full-length MDA5 and MDA5ΔN (Extended Data Figure 7e).

We next investigated how MDA5 filament ICs activate the type I IFN pathway. Previous studies based on crudely purified ICs demonstrated complex uptake by Fc gamma receptors (FcγRs), delivering bound nucleic acids to endosomal TLRs for innate immune activation[28-31]. We first asked whether MDA5ΔN filament ICs are selectively internalized. Indeed, within 4 hours of addition to THP-1 culture medium, filament ICs—but not monomeric ICs—were efficiently cleared from the extracellular compartment and instead appeared in the cellular fraction, using both F01 (Figure 2d) and NP6 mAbs (Extended Data Figure 7f). In contrast, F01 Fab fragments failed to induce intracellular uptake (Figure 2d) or IFN-β production (Figure 2c), consistent with a requirement for Fc-mediated uptake and/or antibody-mediated filament aggregation. Supporting the importance of FcγRs, FcγR blockade also inhibited filament IC-mediated interferon induction (Figure 2e), with the strongest effect observed with blockade of high affinity FcγRI (CD64) (Extended Data Figure 7g). Genetic perturbation further revealed that both dsRNA-sensing TLR3 (with the adaptor TRIF) and RLR (with MAVS) contributed to signaling (Figure 2f), suggesting that dsRNA within ICs can access both the endosome and cytoplasm.

Because THP-1 macrophage activation required all three components (MDA5, dsRNA, and Ab), we next tested how stoichiometry influences signaling output. We also compared NP6 (class I) and NP8 (class II) mAbs, which share similar filament affinities but differ in monomeric binding and filament aggregation (Figure 1). The comparison showed that their signaling activities are strongly dependent on the precise filament assembly condition and antibody binding modes. When MDA5 was predominantly filamentous with a slight excess amount of dsRNA (MDA5:dsRNA binding-site ratio 0.83:1), NP6 outperformed NP8 despite similar filament-binding affinities (Figure 2g, left). Similarly, F01 (class I) was significantly more potent than F12 (class II) under the same condition (Figure 2c). These differences correlate with the enhanced filament-bridging capacity of class I mAbs, which promote the formation of supramolecular ICs with increased valency (Figure 1h, Extended Data Figure 4d). Consistent with the importance of filament bridging by Abs, NP6 titration revealed a bell-shaped signaling curve (Figure 2g, left), likely reflecting excess antibody saturating filaments and preventing crosslinking.

In contrast, when MDA5 was largely monomeric with an excess of MDA5 over dsRNA (MDA5:dsRNA binding-site ratio of 8.3:1), NP8 was more potent than NP6 (Figure 2g, right), with intermediate effects observed at an intermediate ratio (2.8:1, Figure 2g, center). This likely reflects sequestration of NP6 by excess monomeric MDA5, effectively diluting its ability to engage filaments. Such Ab sequestration occurs less for NP8 due to its inefficient binding to monomeric MDA5, explaining its relative dominance under monomer-rich conditions. Consistent with the notion that NP6 antibody is limiting under these conditions, NP6 titration did not result in bell-shaped dose response, in contrast to the filament-dominant condition (Figure 2g).

Together, these data demonstrate that anti-MDA5 autoantibodies activate type I and II interferon signaling only when MDA5 autoantibodies are bound to filamentous MDA5. This activity is amplified when antibodies crosslink filaments into higher-order aggregates, but it is diminished when excess RNA-free MDA5 sequesters antibodies. This illustrates that antibody binding mode and immune complex architecture, rather than affinity alone, determines immunological outcome.

MDA5 filament immune complexes activate inflammatory cell death pathways.

We next asked whether exogenously added MDA5 filament ICs can also activate immunological cell death pathways, given that uptake of large particulate or aggregated stimuli is known to activate inflammasomes and induce pyroptosis in macrophages[32-35]. Interestingly, genes involved in pyroptosis (including *CASP1* and *GSDMD*) as well as other cell death pathways were upregulated in THP-1 macrophages upon MDA5 filament IC stimulation (Figure 3a), suggesting priming for inflammatory death. Immunofluorescence analyses showed increased fraction of cells with ASC specks upon stimulation of THP-1 macrophage with MDA5 filament ICs, but not with monomeric ICs (Figure 3b, 3c). Some cells displayed one bright ASC speck, as reported with commonly used inflammasome stimuli, while others showed multiple ASC specks within individual cells (Figure 3c). Consistent with enhanced pyroptosis, we also observed an increase in IL-1b release (Figure 3d).

Previous studies have implicated neutrophil extracellular traps (NETs) and the associated cell death pathway NETosis in the pathogenesis of anti-MDA5 DM[11,36,37]. We thus asked whether MDA5 ICs, in particular filament ICs, can also activate neutrophils and induce NETosis. Using neutrophils freshly isolated from healthy individuals, we measured NETosis by staining extracellular DNA, myeloperoxidase (MPO), and citrullinated histone H3 (H3Cit), which are found in NETs released from neutrophils. Although basal levels of cells with NETs varied among donors (<1–8%), in all cases, filamentous MDA5 ICs robustly induced NETosis with both NP6 and NP8, whereas monomeric ICs had no measurable effect (Figure 3e-g, Extended Data Figure 8a, 8b). Importantly, removal of any single component of the filament IC (MDA5, RNA, or antibody) abolished NETosis induction (Figure 3e-g, Extended Data Figure 8a, 8b).

Together, these results demonstrate that MDA5 filament ICs also activate inflammatory cell death pathways, including pyroptosis and NETosis, highlighting their potential role in amplifying immune pathology.

MDA5 filament ICs are enriched in anti-MDA5 DM patient plasma.

Since MDA5 filament ICs robustly activate interferon signaling and NET release, both of which are key features of anti-MDA5 DM, we hypothesized that these filament ICs would be present in the peripheral blood of anti-MDA5 DM patients. To detect MDA5 filaments in human samples, we developed a sandwich ELISA that discriminates between monomeric and filamentous MDA5 by leveraging TRIM65's selective recognition of filamentous MDA5[21] (Figure 4a). Recombinant TRIM65 was immobilized on plates, incubated with MDA5 as monomers or filaments, and then probed using anti-MDA5 antibodies (1˚ Ab, NP8 or F01), followed by anti-human secondary IgG (2˚ Ab, Figure 4b). Proof-of-principle testing revealed that, regardless of the specific 1˚ Ab used, TRIM65 ELISA detects MDA5 filament with a 60-80-fold higher sensitivity than MDA5 monomers (Figure 4b, Extended Data Figure 8c).

We examined plasma from a panel of 4 healthy controls (HCs) and 19 individuals diagnosed with dermatomyositis[38], 16 of whom were positive for anti-MDA5 antibodies by clinical testing (Extended Data Table 3). Most patients were actively treated, most commonly with intravenous immunoglobulin and/or mycophenolate mofetil (Extended Data Table 4). Because circulating MDA5 filament ICs may be bound by native anti-MDA5 antibodies, thus restricting the capacity of 1˚ Ab to probe extracellular MDA5 filaments, we performed the TRIM65 sandwich ELISA with or without 1˚ Ab incubation (Extended Data Figure 8d). Surprisingly, the absorbance values for samples probed with and without 1˚ Ab were largely similar (Extended Data Figure 8e), suggesting that filament ICs in plasma were either saturated with native anti-MDA5 antibodies, and/or these complexes included antibodies that may not directly bind MDA5 filaments.

Analysis of ELISA data in which 1˚ Ab was omitted showed that anti-MDA5 DM patients with active disease at the time of blood draw had elevated levels of MDA5 filament ICs, but this was attenuated by glucocorticoid use (Figure 4c). Anti-MDA5 DM patients with quiescent disease and anti-MDA5-negative individuals generally had less peripheral MDA5 filament ICs. We also determined the levels of anti-MDA5 antibody using an direct ELISA against MDA5 (Figure 4d) and found that these titers were also elevated in anti-MDA5 DM patients with active disease, consistent with prior reports[39,40], but did not correlate with glucocorticoid use. Notably, MDA5 filament IC levels in this group were uniformly low and showed minimal variability despite substantial fluctuations in circulating anti-MDA5 antibodies, raising the possibility that the biogenesis of MDA5 filament and/or their extracellular release is steroid-responsive.

To further examine the relationship between disease course and circulating MDA5 filament ICs and autoantibodies, three anti-MDA5 DM subjects with active disease (P12, P15, P18) were followed longitudinally with subsequent disease remission or progression. In both P12 and P15, clinical remission was accompanied by reductions in circulating MDA5 filament ICs and autoantibody levels, whereas both increased in P18 during disease progression (Figure 4e, 4f). These data collectively suggest a close relationship between circulating MDA5 filament ICs and disease activity, consistent with their pathogenic role in anti-MDA5 DM.

LINE-derived dsRNAs are enriched in anti-MDA5 DM patient plasma.

Given that MDA5 filament formation requires dsRNA, the presence of MDA5 filament in patient plasma raised the question of which RNA species might drive this process. Direct identification of MDA5-bound dsRNA, such as by RNase protection assay[15], would require large sample quantities, which is not feasible with available patient plasma. We therefore analyzed total cell-free RNA from plasma, reasoning that unprotected RNA would be rapidly degraded in the nuclease-rich plasma environment. Consistent with this idea, plasma RNA exhibited a markedly shorter size distribution based on electropherogram analysis, compared to cellular RNA isolated from peripheral blood mononuclear cells (PBMCs) (Extended Data Figure 9a).

We performed stranded RNA-seq using total RNA from plasma and PBMCs of healthy controls (HC), anti-MDA5-negative DM (with active disease), anti-MDA5 DM (active), and anti-MDA5 DM (inactive) individuals (Figure 5a). We first started with differential gene expression analysis focusing on annotated genes. Based on PBMC data, anti-MDA5 DM patients showed a strong type I IFN signature relative to HC in PBMC, which is consistent with previous reports[8-10]. This IFN signature was somewhat attenuated, with substantial inter-individual variability, in anti-MDA5 DM (inactive) patients and non-MDA5 DM (active) patients. In contrast to the PBMC RNA, plasma RNA showed no broad IFN signature in either anti-MDA5 DM or non-MDA5 DM patients, consistent with the degradation of most mRNAs. Certain mitochondrial genes were modestly enriched in some of the patient plasma, but there was no strong correlation between disease type or activity with mitochondrial RNA (Extended Data Figure 9b).

We next expanded our analysis to all genomic loci, including unannotated intergenic regions, to identify RNA species enriched in patient plasma. Because plasma RNA is highly fragmented, we used a peak-calling strategy to identify differentially enriched regions in patients versus HCs, regardless of gene annotation (Extended Data Figure 9c). This analysis revealed long interspersed nuclear elements (LINEs), common retroelements constituting ~17% of the genome that are normally transcriptionally silenced[41,42], as the most prominently enriched species. That is, LINEs showed both high fold-change and high abundance in plasma RNA from anti-MDA5 DM patients P15 and P12 (relative to HC1/2), but not from anti-MDA5-negative DM P11 or P13 (Extended Data Figure 9c). To systematically examine this pattern, fold-changes of all LINE reads arising from loci that are differentially regulated in individual patients over HC1/2 were plotted in heatmaps (Figure 5b). As most LINE reads cannot be mapped uniquely in the genome, primary mapping (random assignment among best loci) was used.

The results showed that anti-MDA5 DM patients, regardless of disease activity or steroid use, showed strong LINE upregulation in plasma. Unlike LINEs, neither short interspersed nuclear elements (SINEs) nor endogenous retroviruses (ERVs) showed similar upregulation in patient plasma. In PBMCs, by contrast, only anti-MDA5 DM patients with active disease showed upregulation of LINEs (Figure 5b). Further supporting a link between LINEs and disease activity, longitudinal analysis of patients

P12 and P15 showed that LINE levels in both plasma and PBMC declined with clinical improvement (Figure 5c). These findings suggest that LINE-derived RNAs may contribute to anti-MDA5 DM pathogenesis, though its level does not strictly correlate across different patients.

We next examined whether these upregulated LINE transcripts form dsRNA. To address this, we quantified sense and antisense LINE RNAs, reasoning that duplex formation would result in comparable abundance of both strands. Reads were mapped strand-specifically to the collection of LINE reference sequences representing ~40 subfamilies spanning different evolutionary ages. The most enriched LINE transcripts belonged to L1HS, the youngest and most transcriptionally active L1 subfamily[41,42], in both PBMCs and plasma RNA from patient P15 (Figures 5d). These were followed by L1PA2-8, which are closely related to L1HS (Extended Data Figure 9d). In plasma, L1HS reads in the sense and antisense orientations were present at nearly equivalent levels (sense-to-antisense ratio ~1.1), whereas in PBMCs, sense transcripts were more abundant (sense-to-antisense ratio ~5.2) (Figures 5d). This pattern is consistent with the idea that antisense LINE RNAs are preferentially stabilized in plasma through duplex formation. A similar trend was observed in P12 (Extended Data Figure 9e). Notably, after remission, both sense and antisense reads of LINE RNAs were markedly reduced in both P15 and P12 (Figure 5d, Extended Data Figure 9e), further supporting the link between LINE RNAs and disease pathogenesis.

To further validate dsRNA formation by sense and antisense LINE RNAs, we quantified adenosine-to-inosine (A-to-I) editing, which is catalyzed by ADAR1 and occurs specifically on dsRNA[3]. Because inosines are reverse transcribed as guanosines, A-to-I editing can be detected as A-to-G mismatches between sequencing reads and the reference genome (Figure 5e). To minimize artifacts from misalignment, we restricted the analysis to reads that could be uniquely mapped to single genomic loci. We found that reads with A-to-I editing were significantly elevated in active anti-MDA5 DM patients (P12 and P15) than HC1/2 or anti-MDA5-negative DM patients (P7 and P8) (Figure 5f, upper panel). These are bona fide A-to-I edits rather than mapping errors as they were present at a vastly higher rate than other types of mismatches (Figure 5f). Additionally, they are not A-to-G single nucleotide polymorphisms, as the mismatches were present stochastically across reads, consistent with post-transcriptional editing rather than genomic variation (Figure 5e). A-to-I editing was significantly higher in plasma than in PBMCs (Figures 5f, lower panel), keeping with the notion that LINE-derived dsRNAs are enriched in circulation relative to other RNA. Importantly, the A-to-I editing levels in P12 and P15 decreased upon clinical remission (Figure 5f), supporting a link between dsRNA formation and disease activity.

Although extensive A-to-I editing can destabilize dsRNA and disrupt MDA5 filament formation[15], the observed editing frequency on LINE RNAs (approximately 2 edits per 100 bp on average) is unlikely to impair MDA5 activation, particularly given the strong sequence conservation of L1HS that would enable stable sense-antisense duplex formation. This notion is supported by a previous observation that MDA5 can tolerate ~4 bp mismatches within 112 bp dsRNA[43]. In contrast to L1HS sense-antisense duplex, other types of common endogenous dsRNA like IR-Alus contain ~20% mismatches within the duplex region even prior to A-to-I editing[15], which would be further destabilized by A-to-I editing.

Altogether, these data suggest that LINE-derived dsRNAs are enriched in patients specifically with anti-MDA5 DM, not non-MDA5 DM or healthy controls, and the level of both plasma and PBMC LINE dsRNA decreases with disease remission.

LINE-derived RNAs are induced by immune stimulation.

We next asked why LINE-derived RNAs are upregulated in anti-MDA5 DM patients. We investigated the genomic source of patient-enriched LINEs, focusing on uniquely mappable LINE reads to accurately assign genomic origin. Because the small size of plasma RNA severely limits unique mapping, we performed this analysis using PBMC RNA-seq data. Patient-enriched, uniquely mapped LINEs were categorized into 6 groups (intergenic, intron, CDR, 5' UTR, 3' UTR, <3kb upstream and downstream of genes), weighted with their read abundance (see Methods). In the human genome, L1HS, which dominated LINE signal in P15 and P12, are primarily located in intergenic regions (47%) and introns (45%) (Figure 6a, left). In contrast, in P15 (Figure 6a) and P12 (Extended Data Figure 10a), LINE reads showed a marked shift towards gene-proximal regions: contributions from 3' UTR and upstream region increased from 5-10% to nearly 50%, for both sense and antisense LINE reads. When restricting the analysis to highly expressed LINE loci (>200 uniquely mapped normalized reads), 3' UTRs became the most dominant source of antisense LINE reads, whereas both 3' UTR and upstream regions dominated for sense LINEs.

Interestingly, in analysis of the orientation of LINE reads relative to the host or nearby gene, LINE read orientation was strongly biased by host gene orientation in all gene-proximal categories: LINE reads were predominantly co-directional with the host transcript, such that antisense LINE reads were enriched when the LINE orientation opposed the gene direction, and vice versa for sense LINEs (Figure 6a, Extended Data Figure 10a). These results suggest that LINE transcription is largely driven by host or nearby gene transcription rather than autonomous LINE promoters.

To further test this idea, we examined LINE expression at individual loci in healthy control PBMCs (HC1/2) versus P15 (Figure 6b) or P12 PBMCs (Extended Data Figure 10b), while categorizing LINEs based on proximity to genes that were upregulated (red), downregulated (blue), unchanged (gray), or located >3 kb away from genes (black). Highly expressed LINEs were predominantly located near genes, and those showing the strongest upregulation tended to lie adjacent to genes that were themselves upregulated in anti-MDA5 DM. Pathway analysis of genes near top 100 upregulated LINEs in P15 (Figure 6c) and P12 (Extended Data Figure 10c) revealed enrichment for immune-related pathways, including interferon signaling—a hallmark of anti-MDA5 DM[8-10] and a signature also observed in our THP-1 model (Figure 2b).

To determine whether innate immune stimulation with MDA5 filament ICs alone can result in LINE induction, we reanalyzed THP-1 RNA-seq data from Figure 2a with a focus on repetitive elements. Notably, THP-1 macrophages stimulated with filamentous MDA5 ICs, but not with monomeric MDA5 ICs, showed robust upregulation of LINEs, whereas upregulation of SINEs or ERVs were minimal (Figure 6d). As in patient PBMCs, LINE induction was strongly biased toward elements located within or near genes that were transcriptionally upregulated (Figure 6e), many of which are again involved in innate immune signaling (Figure 6f).

Together, these findings indicate that LINE upregulation in anti-MDA5 DM and upon MDA5 filament IC activation is largely driven by host gene transcription, particularly innate immune programs, providing a mechanistic link between inflammation and biogenesis of endogenous dsRNA ligands.

Discussion

Previous studies of IFN-driven autoimmune diseases, mainly SLE[44], led to the prevailing model that nucleic acid-binding autoantigens in complex with autoantibodies engage FcγRs and deliver immunostimulatory nucleic acids to endosomal TLRs[28-31,45], thus activating endogenous IFN pathways[46,47]. While these studies implicated extracellular nucleic acids in disease pathogenesis, their exact identity, molecular architecture and functional determinants of pathogenic ICs have remained incompletely defined in many cases.

Using four monoclonal autoantibodies isolated from anti-MDA5 DM patients, we reconstitute pathogenic ICs from fully purified components—MDA5, RNA, and antibody—enabling direct biochemical, structural, and cellular functional assays. This approach reveals that RNA functions not only as a ligand for innate immune receptors but also as a structural scaffold for antigen multimerization, and that autoantibodies are not merely passive adaptors linking autoantigens to FcγRs, but actively shape antigen oligomeric state through aggregation. As a result, antibody binding mode, stoichiometry and assembly architecture of the ICs, beyond antibody affinity, govern immune-stimulatory activity. This architectural principle is likely relevant to other autoimmune diseases involving antibodies against intracellular nucleic acid-binding proteins[48,49]. The resulting ICs are highly pathogenic in that they activate a broad range of innate immune pathways, including type I and II interferon signaling, pyroptosis and NETosis. Released proinflammatory cytokines would drive leukocyte recruitment and local tissue inflammation, while NETs may impair wound healing. These observations together provide a mechanistic explanation for lung pathology and cutaneous ulceration[8-10].

Applying cell-free RNA-seq identifies LINE-derived dsRNA as a key extracellular component of pathogenic MDA5 ICs. The role and source of LINE RNAs in anti-MDA5 DM differ fundamentally from those described in cancer and other disease contexts, where autonomous LINE activation is viewed primarily as a biomarker of epigenetic dysregulation, or as a driver of genomic instability and cGAS–STING signaling through LINE-encoded enzymatic activities[50,51]. In contrast, in anti-MDA5 DM, LINEs function through stable dsRNA formation generated non-autonomously by host or nearby gene transcription. Because many inflammatory genes harbor LINE elements, immune activation by MDA5 ICs further amplifies LINE dsRNA expression. As MDA5 itself is also induced as an interferon-stimulated gene, this would likely promote additional filament formation and their extracellular release through inflammatory cell death, establishing a self-amplifying feed-forward loop that drives disease propagation (Figure 6g).

Notably, extracellular enrichment of LINE dsRNA was specific to anti-MDA5 DM, and was not shared with non-MDA5 DM, probably reflecting stabilization of LINE dsRNA by MDA5 filament formation and IC assembly. In contrast, inverted-repeat Alu dsRNAs, which are often a major intracellular source of MDA5 ligands[15-17], were not prominent extracellularly, likely due to imperfect duplex complementarity that limits stability in the nuclease-rich plasma environment. Thus, pathogenic extracellular nucleic acids that scaffold intracellular autoantigens may differ from intracellular counterparts because of strong extracellular selection for stability, a principle that may extend to other autoantigen systems.

The initiating trigger of the pathogenic vicious cycle––the source of initiating dsRNA–– remains uncertain. Viral dsRNA represents one plausible trigger and may help explain the pulmonary symptoms, seasonal disease flares, and the detection of anti-MDA5 antibodies in subsets of COVID-19 patients[6,10]. However, we did not detect enrichment of viral RNA from anti-MDA5 DM patient plasma compared to healthy controls, which may reflect that persistence of the initiating stimulus may not be required once the inflammatory circuit is established.

Finally, our structural analyses reveal striking epitope convergence across unrelated patients. Class I antibodies recognize the same MDA5 epitope through germline-encoded light chain residues despite divergent heavy chains and CDR3 sequences, while class II antibodies recognize yet another epitope in MDA5 using the identical heavy and light chain genes with minimal somatic mutations. These two incidences of convergence suggests that MDA5 harbors epitopes with an intrinsic predisposition to breach B cell tolerance, reminiscent of germline-driven immunodominance described in antiviral immunity[26]. Future research is necessary to determine the potential role of immunodominance in anti-MDA5 DM and other autoimmune diseases.

Altogether, our findings define anti-MDA5 DM as a “perfect storm” in which both innate and adaptive immune tolerance are breached, resulting in a self-sustaining pathogenic inflammatory loop. More broadly, this work provides a molecular architectural framework for understanding how intracellular nucleic acid-binding proteins can become potent extracellular immunogens.

1 Sato, S. *et al.* Autoantibodies to a 140-kd polypeptide, CADM-140, in Japanese patients with clinically amyopathic dermatomyositis. *Arthritis Rheum* **52**, 1571-1576 (2005). https://doi.org:10.1002/art.21023

2 Sato, S. *et al.* RNA helicase encoded by melanoma differentiation-associated gene 5 is a major autoantigen in patients with clinically amyopathic dermatomyositis: Association with rapidly progressive interstitial lung disease. *Arthritis Rheum* **60**, 2193-2200 (2009). https://doi.org:10.1002/art.24621

3 Hur, S. Double-Stranded RNA Sensors and Modulators in Innate Immunity. *Annu Rev Immunol* **37**, 349-375 (2019). https://doi.org:10.1146/annurev-immunol-042718-041356

4 Kurtzman, D. J. B. & Vleugels, R. A. Anti-melanoma differentiation-associated gene 5 (MDA5) dermatomyositis: A concise review with an emphasis on distinctive clinical features. *J Am Acad Dermatol* **78**, 776-785 (2018). https://doi.org:10.1016/j.jaad.2017.12.010

5 Lundberg, I. E. *et al.* Idiopathic inflammatory myopathies. *Nat Rev Dis Primers* **7**, 86 (2021). https://doi.org:10.1038/s41572-021-00321-x

6 Lu, X., Peng, Q. & Wang, G. Anti-MDA5 antibody-positive dermatomyositis: pathogenesis and clinical progress. *Nat Rev Rheumatol* **20**, 48-62 (2024). https://doi.org:10.1038/s41584-023-01054-9

7 Selva-O'Callaghan, A. *et al.* Pharmacologic Treatment of Anti-MDA5 Rapidly Progressive Interstitial Lung Disease. *Curr Treatm Opt Rheumatol* **7**, 319-333 (2021). https://doi.org:10.1007/s40674-021-00186-x

8 Ye, Y. *et al.* Single-cell profiling reveals distinct adaptive immune hallmarks in MDA5+ dermatomyositis with therapeutic implications. *Nat Commun* **13**, 6458 (2022). https://doi.org:10.1038/s41467-022-34145-4

9 Yoshida, A. *et al.* Dysregulated type I/III interferon system in circulation from patients with anti-MDA5-positive dermatomyositis. *Sci Rep* **15**, 25537 (2025). https://doi.org:10.1038/s41598-025-10895-1

10 Yoshida, T. & Nakashima, R. Anti- Melanoma Differentiation-Associated Gene 5 Antibody Positive Dermatomyositis: Recent Progress in Pathophysiology and Treatment. *Curr Rheumatol Rep* **27**, 23 (2025). https://doi.org:10.1007/s11926-025-01188-7

11 Seto, N. *et al.* Neutrophil dysregulation is pathogenic in idiopathic inflammatory myopathies. *JCI Insight* **5** (2020). https://doi.org:10.1172/jci.insight.134189

12 Ichimura, Y. *et al.* Autoimmunity against melanoma differentiation-associated gene 5 induces interstitial lung disease mimicking dermatomyositis in mice. *Proc Natl Acad Sci U S A* **121**, e2313070121 (2024). https://doi.org:10.1073/pnas.2313070121

13 Pinal-Fernandez, I. *et al.* Pathogenic autoantibody internalization in myositis. *medRxiv* (2024). https://doi.org:10.1101/2024.01.15.24301339

14 Ablasser, A. & Hur, S. Regulation of cGAS- and RLR-mediated immunity to nucleic acids. *Nat Immunol* **21**, 17-29 (2020). https://doi.org:10.1038/s41590-019-0556-1

15 Ahmad, S. *et al.* Breaching self-tolerance to Alu duplex RNA underlies MDA5-mediated inflammation *Cell* **172**, 797-810 (2018).

16 Mehdipour, P. *et al.* Epigenetic therapy induces transcription of inverted SINEs and ADAR1 dependency. *Nature* **588**, 169-173 (2020). https://doi.org:10.1038/s41586-020-2844-1

17 Sun, T. *et al.* ADAR1 editing is necessary for only a small subset of cytosolic dsRNAs to evade MDA5-mediated autoimmunity. *Nat Genet* **57**, 3101-3111 (2025). https://doi.org:10.1038/s41588-025-02430-9

18 Peisley, A. *et al.* Cooperative assembly and dynamic disassembly of MDA5 filaments for viral dsRNA recognition. *Proc Natl Acad Sci U S A* **108**, 21010-21015 (2011). https://doi.org:10.1073/pnas.1113651108

19 Berke, I. C., Yu, X., Modis, Y. & Egelman, E. H. MDA5 assembles into a polar helical filament on dsRNA. *Proc Natl Acad Sci U S A* **109**, 18437-18441 (2012).

20 Wu, B. *et al.* Structural Basis for dsRNA Recognition, Filament Formation, and Antiviral Signal Activation by MDA5. *Cell* **152**, 276-289 (2013).

21 Kato, K. *et al.* Structural analysis of RIG-I-like receptors reveals ancient rules of engagement between diverse RNA helicases and TRIM ubiquitin ligases. *Mol Cell* **81**, 599-613 e598 (2021). https://doi.org:10.1016/j.molcel.2020.11.047

22 Hou, F. *et al.* MAVS forms functional prion-like aggregates to activate and propagate antiviral innate immune response. *Cell* **146**, 448-461 (2011). https://doi.org:10.1016/j.cell.2011.06.041

23 Crow, Y. J. & Stetson, D. B. The type I interferonopathies: 10 years on. *Nat Rev Immunol* **22**, 471-483 (2022). https://doi.org:10.1038/s41577-021-00633-9

24 van Gompel, E. *et al.* Anti-MDA5 monoclonal antibodies from patients with dermatomyositis - B cell characteristics and differential targeting of the helicase domains. *BioRxiv* (2025). https://doi.org:https://doi.org/10.64898/2025.12.01.691530

25 Rice, G. I. *et al.* Gain-of-function mutations in IFIH1 cause a spectrum of human disease phenotypes associated with upregulated type I interferon signaling. *Nat Genet* **46**, 503-509 (2014). https://doi.org:10.1038/ng.2933

26 Shrock, E. L. *et al.* Germline-encoded amino acid-binding motifs drive immunodominant public antibody responses. *Science* **380**, eadc9498 (2023). https://doi.org:10.1126/science.adc9498

27 Yu, Q., Qu, K. & Modis, Y. Cryo-EM Structures of MDA5-dsRNA Filaments at Different Stages of ATP Hydrolysis. *Mol Cell* **72**, 999-1012 e1016 (2018). https://doi.org:10.1016/j.molcel.2018.10.012

28 Wu, Y. *et al.* TLR7/8 Activation in Immune Cells and Muscle by RNA-Containing Immune Complexes: Role in Inflammation and the Pathogenesis of Myositis. *Arthritis Rheumatol* **77**, 190-201 (2025). https://doi.org:10.1002/art.42989

29 Eloranta, M. L. *et al.* A possible mechanism for endogenous activation of the type I interferon system in myositis patients with anti-Jo-1 or anti-Ro 52/anti-Ro 60 autoantibodies. *Arthritis Rheum* **56**, 3112-3124 (2007). https://doi.org:10.1002/art.22860

30 Vollmer, J. *et al.* Immune stimulation mediated by autoantigen binding sites within small nuclear RNAs involves Toll-like receptors 7 and 8. *J Exp Med* **202**, 1575-1585 (2005). https://doi.org:10.1084/jem.20051696

31 Hung, T. *et al.* The Ro60 autoantigen binds endogenous retroelements and regulates inflammatory gene expression. *Science* **350**, 455-459 (2015).

32 Yazdi, A. S. *et al.* Nanoparticles activate the NLR pyrin domain containing 3 (Nlrp3) inflammasome and cause pulmonary inflammation through release of IL-1alpha and IL-1beta. *Proc Natl Acad Sci U S A* **107**, 19449-19454 (2010). https://doi.org:10.1073/pnas.1008155107

33 Duewell, P. *et al.* NLRP3 inflammasomes are required for atherogenesis and activated by cholesterol crystals. *Nature* **464**, 1357-1361 (2010). https://doi.org:10.1038/nature08938

34 Martinon, F., Petrilli, V., Mayor, A., Tardivel, A. & Tschopp, J. Gout-associated uric acid crystals activate the NALP3 inflammasome. *Nature* **440**, 237-241 (2006). https://doi.org:10.1038/nature04516

35 Halle, A. *et al.* The NALP3 inflammasome is involved in the innate immune response to amyloid-beta. *Nat Immunol* **9**, 857-865 (2008). https://doi.org:10.1038/ni.1636

36 Liu, T. *et al.* Neutrophil-to-lymphocyte ratio is a predictive marker for anti-MDA5 positive dermatomyositis. *BMC Pulm Med* **22**, 316 (2022). https://doi.org:10.1186/s12890-022-02106-8

37 Peng, Y., Zhang, S., Zhao, Y., Liu, Y. & Yan, B. Neutrophil extracellular traps may contribute to interstitial lung disease associated with anti-MDA5 autoantibody positive dermatomyositis. *Clin Rheumatol* **37**, 107-115 (2018). https://doi.org:10.1007/s10067-017-3799-y

38 Bottai, M. *et al.* EULAR/ACR classification criteria for adult and juvenile idiopathic inflammatory myopathies and their major subgroups: a methodology report. *RMD Open* **3**, e000507 (2017). https://doi.org:10.1136/rmdopen-2017-000507

39 Matsushita, T. *et al.* Antimelanoma differentiation-associated protein 5 antibody level is a novel tool for monitoring disease activity in rapidly progressive interstitial lung disease with dermatomyositis. *Br J Dermatol* **176**, 395-402 (2017). https://doi.org:10.1111/bjd.14882

40 Cao, H. *et al.* Clinical manifestations of dermatomyositis and clinically amyopathic dermatomyositis patients with positive expression of anti-melanoma differentiation-associated gene 5 antibody. *Arthritis Care Res (Hoboken)* **64**, 1602-1610 (2012). https://doi.org:10.1002/acr.21728

41 Mendez-Dorantes, C. & Burns, K. H. LINE-1 retrotransposition and its deregulation in cancers: implications for therapeutic opportunities. *Genes Dev* **37**, 948-967 (2023). https://doi.org:10.1101/gad.351051.123

42 Richardson, S. R. *et al.* The Influence of LINE-1 and SINE Retrotransposons on Mammalian Genomes. *Microbiol Spectr* **3**, MDNA3-0061-2014 (2015). https://doi.org:10.1128/microbiolspec.MDNA3-0061-2014

43 Peisley, A. *et al.* Kinetic mechanism for viral dsRNA length discrimination by MDA5 filaments. *Proc Natl Acad Sci U S A* **109**, E3340-3349 (2012). https://doi.org:10.1073/pnas.1208618109

44 Mustelin, T., Lood, C. & Giltiay, N. V. Sources of Pathogenic Nucleic Acids in Systemic Lupus Erythematosus. *Front Immunol* **10**, 1028 (2019). https://doi.org:10.3389/fimmu.2019.01028

45 Marshak-Rothstein, A. & Rifkin, I. R. Immunologically active autoantigens: the role of toll-like receptors in the development of chronic inflammatory disease.

Annu Rev Immunol **25**, 419-441 (2007). https://doi.org:10.1146/annurev.immunol.22.012703.104514

46 Wang, K. *et al.* RNA-Containing Immune Complexes Formed by Anti-Melanoma Differentiation Associated Gene 5 Autoantibody Are Potent Inducers of IFN-alpha. *Front Immunol* **12**, 743704 (2021). https://doi.org:10.3389/fimmu.2021.743704

47 Leadbetter, E. A. *et al.* Chromatin-IgG complexes activate B cells by dual engagement of IgM and Toll-like receptors. *Nature* **416**, 603-607 (2002). https://doi.org:10.1038/416603a

48 Burbelo, P. D., Iadarola, M. J., Keller, J. M. & Warner, B. M. Autoantibodies Targeting Intracellular and Extracellular Proteins in Autoimmunity. *Front Immunol* **12**, 548469 (2021). https://doi.org:10.3389/fimmu.2021.548469

49 Suurmond, J. & Diamond, B. Autoantibodies in systemic autoimmune diseases: specificity and pathogenicity. *J Clin Invest* **125**, 2194-2202 (2015). https://doi.org:10.1172/JCI78084

50 Zhang, X., Zhang, R. & Yu, J. New Understanding of the Relevant Role of LINE-1 Retrotransposition in Human Disease and Immune Modulation. *Front Cell Dev Biol* **8**, 657 (2020). https://doi.org:10.3389/fcell.2020.00657

51 Ardeljan, D., Taylor, M. S., Ting, D. T. & Burns, K. H. The Human Long Interspersed Element-1 Retrotransposon: An Emerging Biomarker of Neoplasia. *Clin Chem* **63**, 816-822 (2017). https://doi.org:10.1373/clinchem.2016.257444

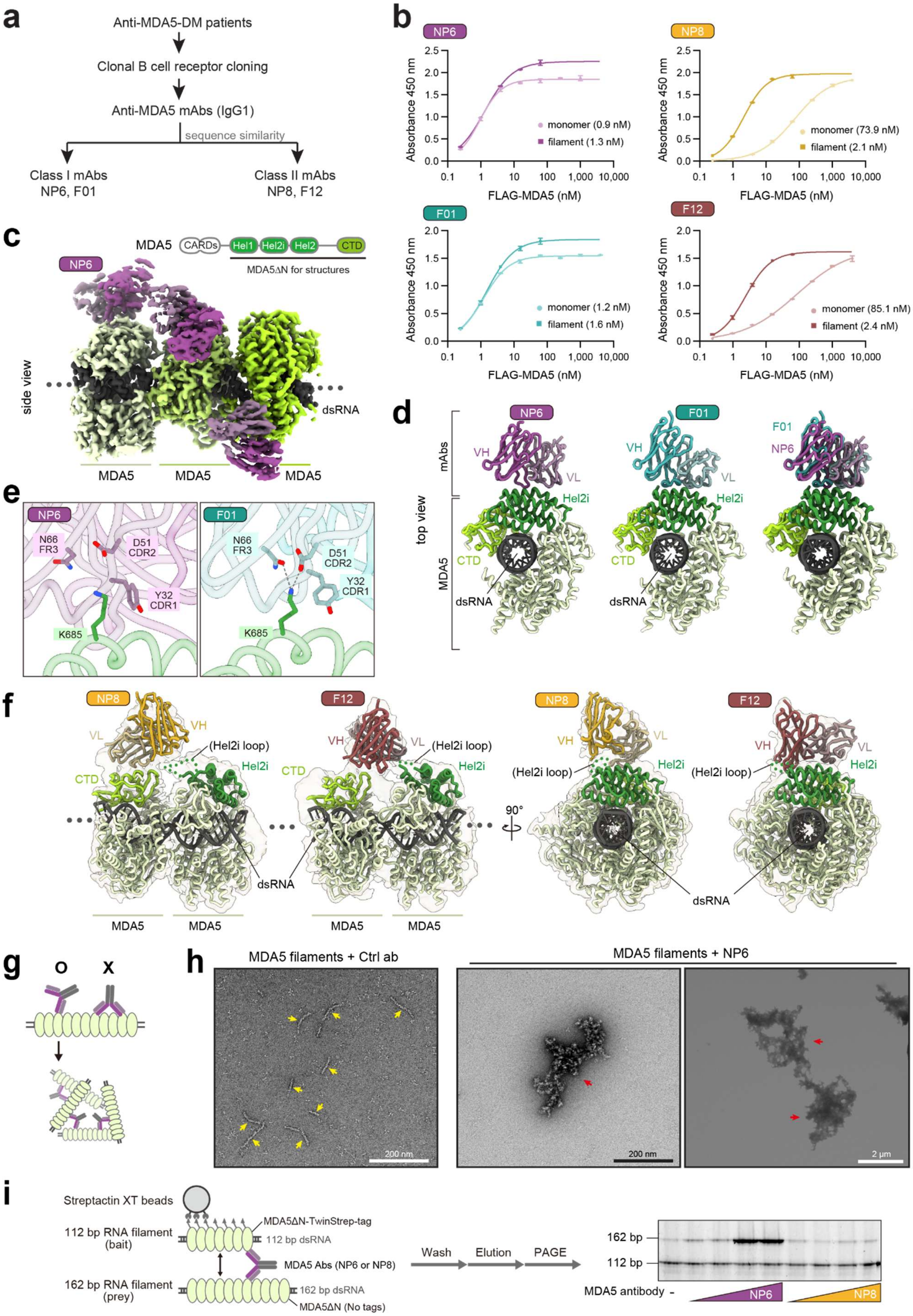
a
Anti-MDA5-DM patients
Clonal B cell receptor cloning
Anti-MDA5 mAbs (IgG1)
sequence similarity
Class I mAbs
NP6, F01
Class II mAbs
NP8, F12
b
NP6
Absorbance 450 nm
FLAG-MDA5 (nM)
monomer (0.9 nM)
filament (1.3 nM)
NP8
monomer (73.9 nM)
filament (2.1 nM)
F01
monomer (1.2 nM)
filament (1.6 nM)
F12
monomer (85.1 nM)
filament (2.4 nM)
0.0
0.5
1.0
1.5
2.0
2.5
0.1
1
10
100
1,000
10,000
c
MDA5
CARDs
Hel1
Hel2i
Hel2
CTD
MDA5ΔN for structures
NP6
side view
dsRNA
MDA5
MDA5
MDA5
d
NP6
F01
F01
NP6
mAbs
VH
VL
Hel2i
CTD
dsRNA
top view
MDA5
e
NP6
N66
FR3
D51
CDR2
Y32
CDR1
K685
F01
N66
FR3
D51
CDR2
Y32
CDR1
K685
f
NP8
VL
VH
(Hel2i loop)
Hel2i
CTD
F12
VH
VL
(Hel2i loop)
Hel2i
CTD
dsRNA
MDA5
MDA5
MDA5
MDA5
90°
NP8
VH
VL
(Hel2i loop)
Hel2i
F12
VH
VL
(Hel2i loop)
Hel2i
dsRNA
g
o
x
h
MDA5 filaments + Ctrl ab
200 nm
MDA5 filaments + NP6
200 nm
2 μm
i
Streptactin XT beads
112 bp RNA filament
(bait)
MDA5ΔN-TwinStrep-tag
112 bp dsRNA
MDA5 Abs (NP6 or NP8)
162 bp RNA filament
(prey)
162 bp dsRNA
MDA5ΔN (No tags)
Wash
Elution
PAGE
162 bp
112 bp
MDA5 antibody
-
NP6
NP8

Figure 1. Patient-derived mAbs bind MDA5 filaments in two distinct modes.

a) Schematic classifying monoclonal IgG1 antibodies derived from two anti-MDA5 DM patients as class I (NP6, F01) or class II (NP8, F12) based on sequence similarity.

b) ELISA binding curves showing class I or class II mAb reactivity to FLAG-MDA5ΔN monomers or filaments, with apparent K_d shown in parentheses. Filaments were formed by incubating FLAG-MDA5ΔN (20 μM) with *in vitro* transcribed 512 bp dsRNA (640 nM). Data is shown as mean ± SD of 2 technical replicates.

c) Cryo-EM density map of the MDA5ΔN (G495R) filament formed on dsRNA in complex with NP6 scFv antibody from a side view. NP6, MDA5ΔN, and dsRNA are colored magenta, green, and gray, respectively. MDA5 filaments were computationally segmented into three monomers for reconstruction. (Upper right) Domain architecture of MDA5.

d) Top view of the central monomeric complex of MDA5ΔN with NP6 (left), F01 (middle), and a superposition of the two mAbs (right). Hel2i and CTD subdomains are colored dark green and yellow green, respectively. NP6 and F01 are colored magenta and cyan, respectively.

e) Close-up view of MDA5 recognition by NP6 (left) and F01 (right). Germline-encoded residues from Abs that interact with K685 of MDA5 are shown as stick model.

f) Cryo-EM structures of MDA5ΔN in complex with class II mAbs. The cryo-EM map was low-pass filtered to 5 Å resolution and is shown at 10% transparency. MDA5 coloring is the same as in (d). NP8 and F12 are colored yellow and red, respectively. The disordered Hel2i loop is indicated by a dashed green line.

g) Cartoon of the two different modes of full-length antibody binding to MDA5. Structural analysis indicates that only one Fab arm of each Ab can engage a given filament at a time (O); two Fab arms cannot simultaneously bind MDA5 molecules within the same filament (X). This geometry could enable antibodies to bridge distinct filaments, promoting inter-filament crosslinking and aggregation.

h) Negative stain images of MDA5 filaments formed by MDA5ΔN (G495R) (111 nM) and 512 bp dsRNA (3.7 nM) bound by isotype control IgG1 or NP6 antibodies (27.8 nM) taken at 25,000x (left two images). (Right) Filaments were formed with 2.7-fold higher protein and RNA concentrations and imaged at low magnification (2,000x) for visualizing larger aggregates. Yellow arrows indicate individual filaments, whereas red arrows indicate filament aggregates.

i) (Left) Schematic of streptactin pull-down to examine antibody-mediated cross-bridging of MDA5 filaments. Filaments formed by MDA5ΔN tagged with TwinStrep-tag (500 nM) on 112 bp dsRNA (1 ng/μl) were incubated with untagged MDA5ΔN filaments (500 nM) assembled on 162 bp dsRNA (1 ng/μl) and mAbs (62.5-500 nM) prior to streptactin pull-down. The bound RNA was extracted and analyzed by native PAGE (right).

Data are representative of independent experiments (*n* = 2 for B, *n* = 3 for H-I).

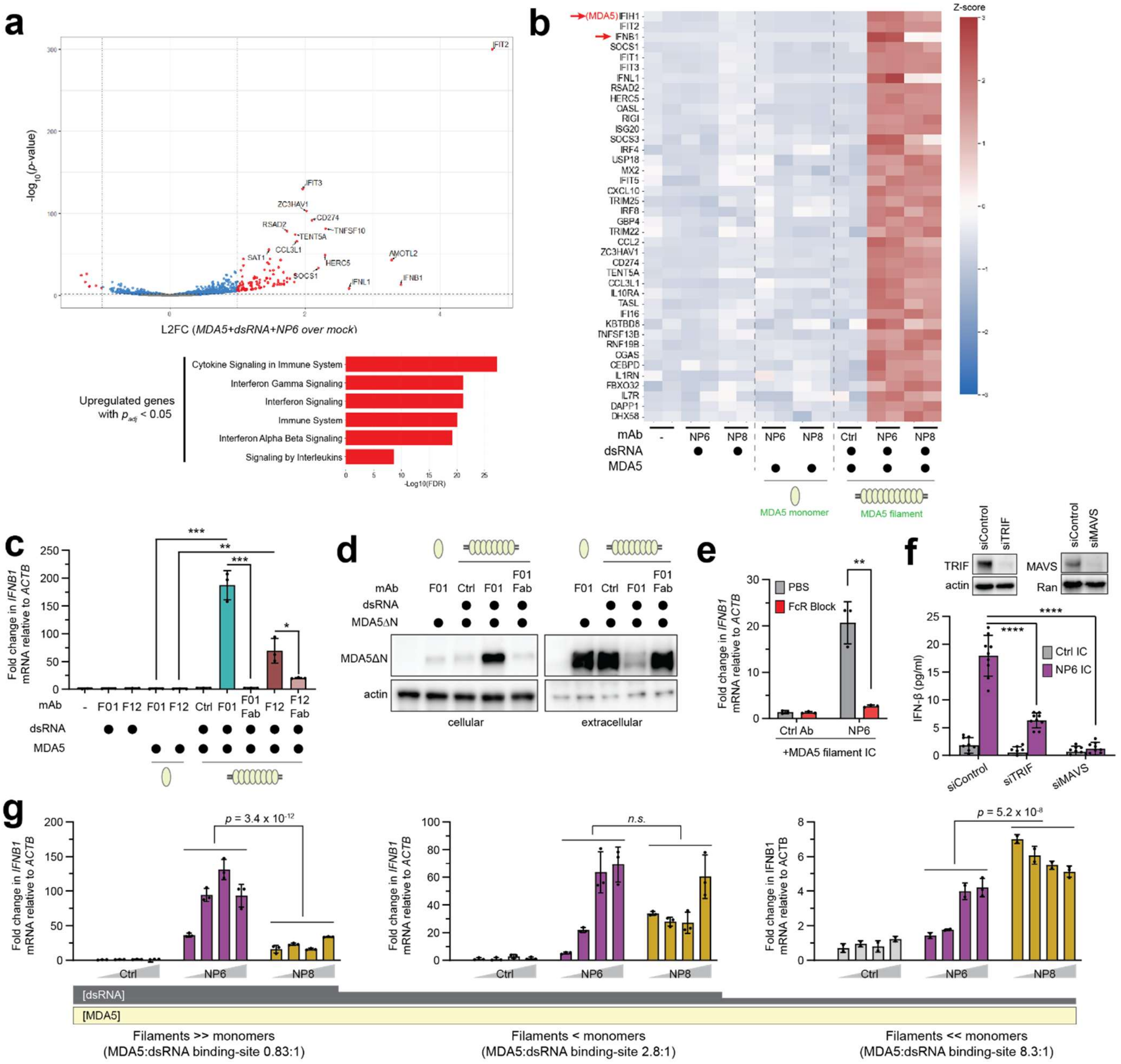

Figure 2. MDA5 filament immune complex activates type I interferon signaling in a binding mode-dependent manner.

a) (Upper) Volcano plot of differentially expressed genes in THP-1-derived macrophages (PMA + IFNγ/LPS) stimulated with MDA5ΔN filament-NP6 ICs over mock. All IC stimulations were performed without the use of intracellular delivery systems. Genes with $\log_2$-fold change |L2FC| >1 with $p < 0.05$ (red) are shown; all other genes shown have $p > 0.05$ (gray) or $p < 0.05$ (blue). (Lower) Reactome pathways of significantly upregulated genes ($p_{adj} < 0.05$, L2FC > 0).

b) Heatmap of *Z*-scored expression of interferon, interferon-stimulated genes, and other immune-related genes in THP-1-derived macrophages stimulated with combinations of MDA5ΔN (90nM monomer), 512 bp dsRNA (3 nM), mAb (NP6/NP8, 90 nM). Ctrl indicates isotype control Ab. *IFIH1* and *IFNB1* are highlighted.

c) *IFNB1* mRNA levels in THP-1-derived macrophages stimulated with combinations of MDA5∆N, dsRNA, mAb (F01/F12, either full-length or Fab) as in (b). Data was normalized to mock treatment. *P*-values were calculated by two-tailed Student's *t* test.

d) Cellular and extracellular MDA5ΔN protein levels in THP-1-derived macrophages stimulated with MDA5ΔN monomer or filament ICs as in (b). 4 hours post-stimulation, supernatant and washed cell pellet were analyzed for MDA5ΔN, which was added extracellularly.

e) *IFNB1* mRNA levels in THP-1 macrophages pre-treated with PBS or Fc block for 1.5 hours, then stimulated with dsRNA-bound MDA5ΔN filaments (13.5 nM; 512 bp dsRNA, 0.45 nM) and NP6 Ab (13.5 nM). *P*-values were calculated by two-tailed Student's *t* test.

f) (Bottom) IFN-β ELISA using THP-1 macrophages electroporated with siRNAs prior to LPS/IFNγ priming and stimulated with dsRNA-bound MDA5ΔN filaments (90 nM; 512 bp dsRNA, 3 nM) and NP6 Ab (90 nM). (Top) Western blot showing knockdown of TRIF and MAVS proteins prior to IC stimulation. *P*-values were calculated by two-tailed Student's *t* test.

g) *IFNB1* mRNA levels in THP-1 macrophages stimulated with ICs composed of NP6/NP8 Abs (90 nM), MDA5ΔN (90 nM), and 512 bp dsRNA (3 nM, left; 0.9 nM, middle; 0.3 nM, right). Data was normalized to mock treatment. *P*-values were calculated by two-way ANOVA to compare NP6 and NP8 IC values across 4 mAb concentrations.

Data are presented as mean ± SD of 3 biological replicates. RNA-seq results contain 2 biological repeats. All other data are representative of at least 3 independent experiments. *$P < 0.05$, **$P < 0.01$, ***$P < 0.001$, ****$P < 0.0001$. *n.s*, not significant.

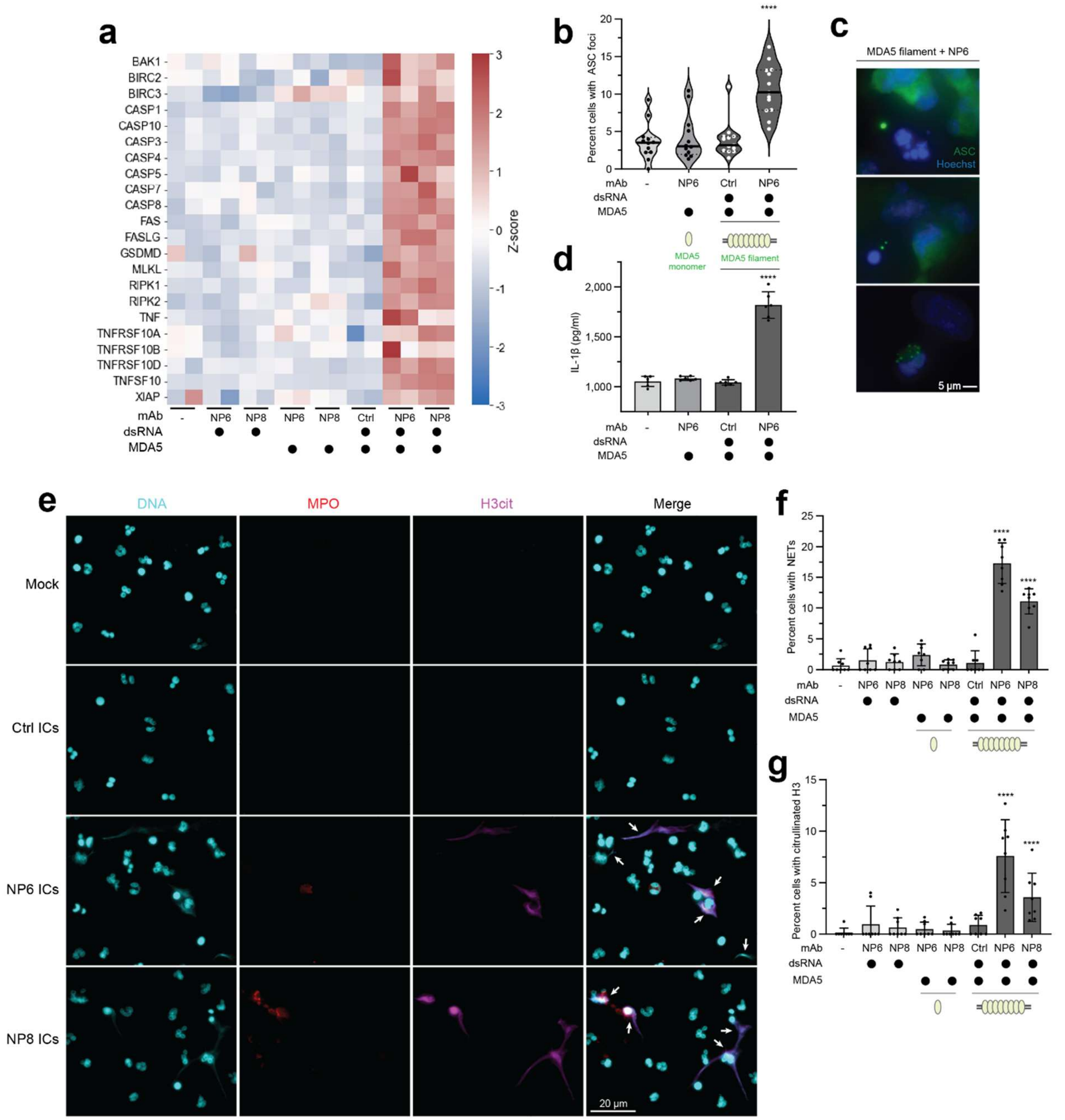

Figure 3. MDA5 filament immune complexes activate inflammatory cell death programs.

a) Heatmap of Z-scored expression of cell death-related genes in THP-1 macrophages stimulated with combinations of NP6/NP8 Abs (90 nM), 512 bp dsRNA (3 nM), and MDA5ΔN (90 nM).
b) ASC foci frequency in THP-1 macrophages stimulated with MDA5ΔN monomer or filament ICs as in (a). Median (solid line) and quartiles (dotted lines) are shown. *P*-values were calculated by one-way ANOVA.
c) Immunofluorescence of ASC foci in THP-1 macrophages stimulated with MDA5ΔN filament ICs as in (a). Nuclei were stained with Hoechst 3342.
d) Secreted IL-1β levels measured by ELISA from THP-1 macrophages stimulated with MDA5ΔN monomer or filament ICs as in (a). *P*-values were calculated by one-way ANOVA.

e) Immunofluorescence analysis of DNA (Hoechst 3342, cyan), myeloperoxidase (MPO, red), citrullinated histone 3 (H3cit, magenta) in healthy human neutrophils stimulated with MDA5ΔN filament ICs (MDA5∆N, 90 nM; 512 bp dsRNA, 3 nM; mAb, 20nM). This experiment was repeated using neutrophils from three different healthy donors, which showed similar patterns (see Extended Data Fig. 8A, 8B).

f) NETosis frequency in neutrophils stimulated as in (e). NETs were defined by extracellular DNA strands or smears co-localizing with MPO and/or H3cit. Four fields of view per well were analyzed. *P*-values were calculated by one-way ANOVA comparing relevant conditions for NP6 or NP8 ICs.

g) Quantitation of citrullinated H3-positive NETs in neutrophils stimulated as in (e). *P*-values were calculated as in (f).

Data are presented as mean ± SD of at least 3 biological replicates. RNA-seq results and neutrophil assays contain 2 biological repeats. All other data are representative of at least 3 independent experiments. $^{*}P < 0.05$, $^{**}P < 0.01$, $^{***}P < 0.001$, $^{****}P < 0.0001$.

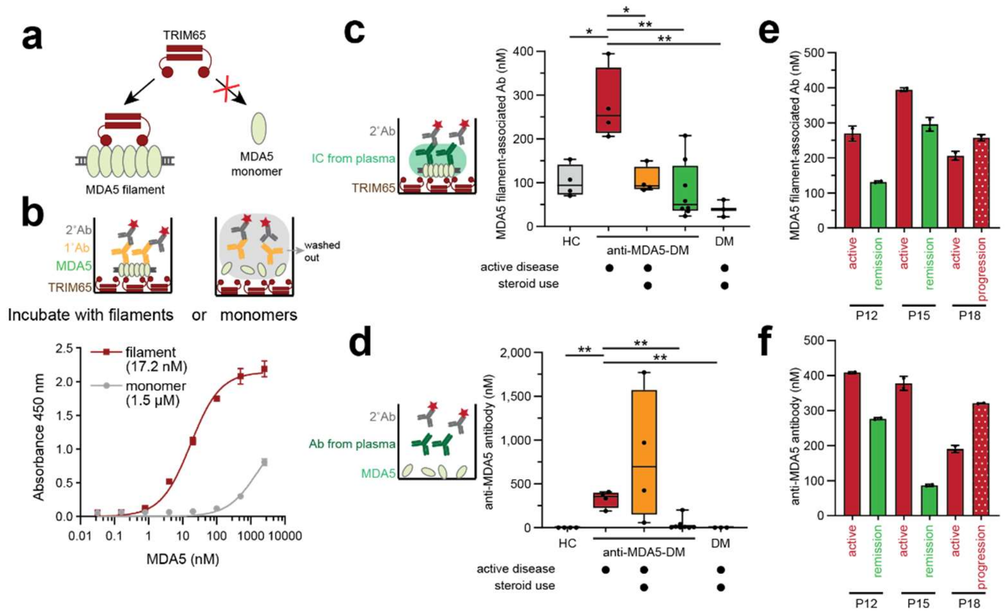

Figure 4. MDA5 filament immune complexes are enriched in anti-MDA5 DM patient plasma.

a) Schematic illustrating TRIM65-mediated selective recognition of MDA5 filaments.

b) Binding curves of TRIM65 to MDA5ΔN monomers or filaments, measured by sandwich ELISA, with apparent K_d shown in parentheses (bottom). Filaments were assembled from MDA5ΔN (5 µM) and 512 bp dsRNA (160 nM). Bound filaments were detected with NP8 mAb (1˚) and anti-human IgG-HRP (2˚) (top)

c) Plasma concentrations of endogenous antibodies bound to MDA5 filaments from individuals diagnosed with anti-MDA5-positive DM with active disease not on glucocorticoid therapy (n = 4), on glucocorticoid therapy (n = 4), anti-MDA5-positive DM with inactive disease (n = 8), anti-MDA5-negative DM (n = 3), or healthy controls (HC) (n = 4). Each data point represents an individual sample with measurements determined by TRIM65 sandwich ELISA, calibrated with a standard curve using recombinant MDA5ΔN filaments. Levels of TRIM65-captured ICs were measured directly with IgG-HRP (2˚) without NP8. See Extended Data Figure 8e for ± NP8 comparison. Disease activity at the time of blood draw was defined by the treating physician and confirmed by a reviewing rheumatologist. *P*-values were calculated by two-tailed Student's *t* test.

d) Plasma anti-MDA5 antibody concentrations determined by direct ELISA using MDA5ΔN-coated plates, calibrated using an NP6 standard curve. See Extended Data Figure 8f.

e-f) Plasma concentrations of MDA5 filament-bound antibody (e) and anti-MDA5 antibody (f) from anti-MDA5 DM individuals during active disease and subsequent remission (P12, P15) or progression (P18).

Data are presented as mean ± SD (n = 2 technical replicates) from at least 3 independent experiments. **P* < 0.05, ***P* < 0.01.

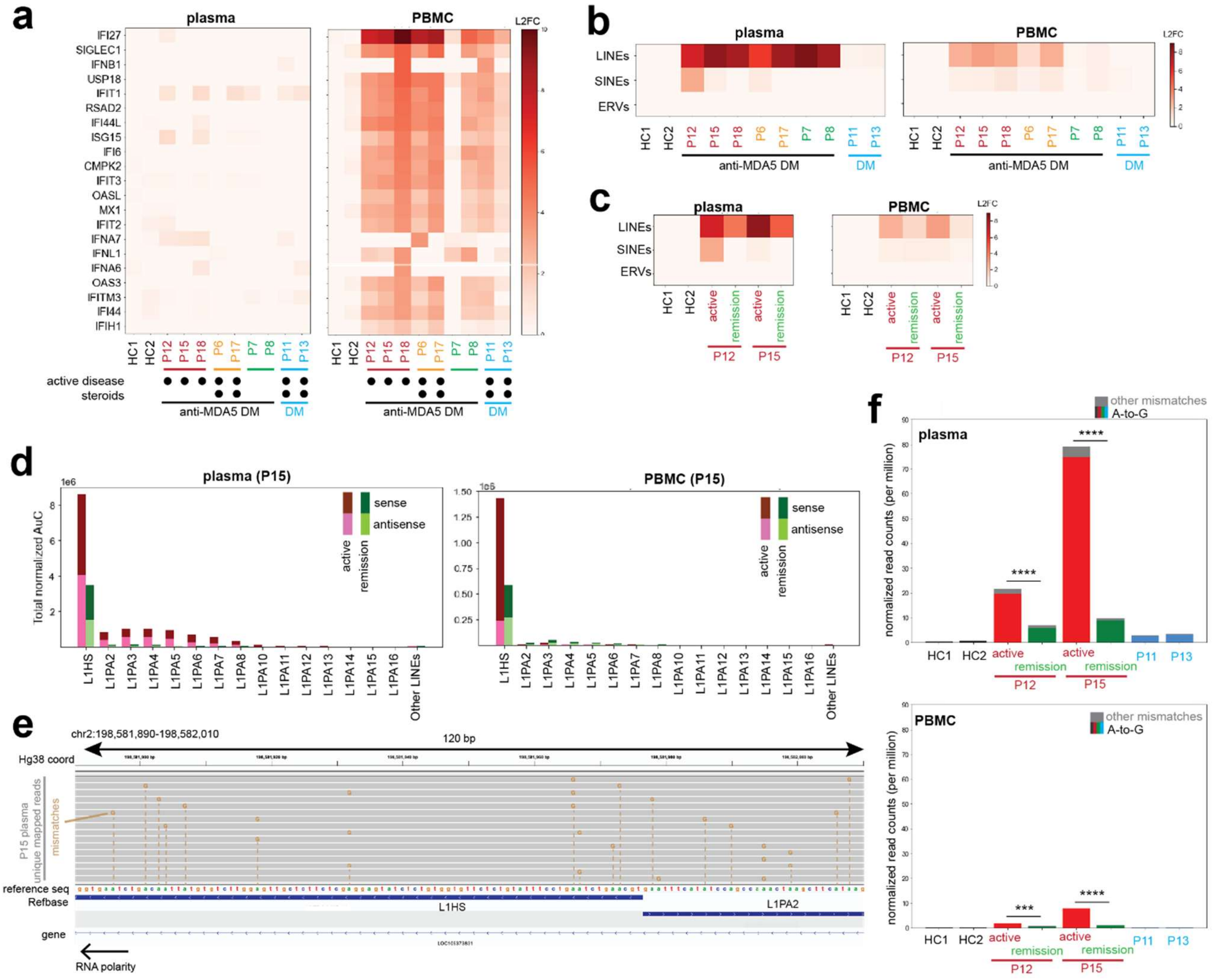

Figure 5. LINE-derived dsRNAs accumulate in anti-MDA5 DM during active disease.

a-b) Heatmaps of the expression of top interferon and interferon-stimulated genes (a) and repeat elements (b) in plasma and PBMC samples. HC, healthy control. All read counts were normalized to the spike-in control.

c) Expression of repeat elements in plasma and PBMC from individuals P12 and P15 during active disease and subsequent disease quiescence.

d) Levels of LINE-1 (L1) and all other LINE elements in plasma (left) and PBMCs (right) from individual P15 during active (red) and quiescent (green) disease. Sense (dark) and antisense (light) sequences are shown.

e) IGV track view of uniquely mappable reads at a representative L1 locus from P15 plasma. Orange nucleotides indicate A-to-G mismatches. No other mismatches were found in these reads.

f) Frequency of reads with A-to-G mismatches and all other mismatches within L1 regions in plasma (upper) and PBMC (lower) samples from healthy controls, anti-MDA5 DM patients during active disease and remission (P12 and P15, red and green), and MDA5-negative DM patients (P11 and P13, blue). Other mismatches are shown in gray. *P*-values were calculated by two-way ANOVA with disease state and patient as factors.

RNA-seq results contain 2 technical repeats. *$P < 0.05$, **$P < 0.01$, ***$P < 0.001$, ****$P < 0.0001$.

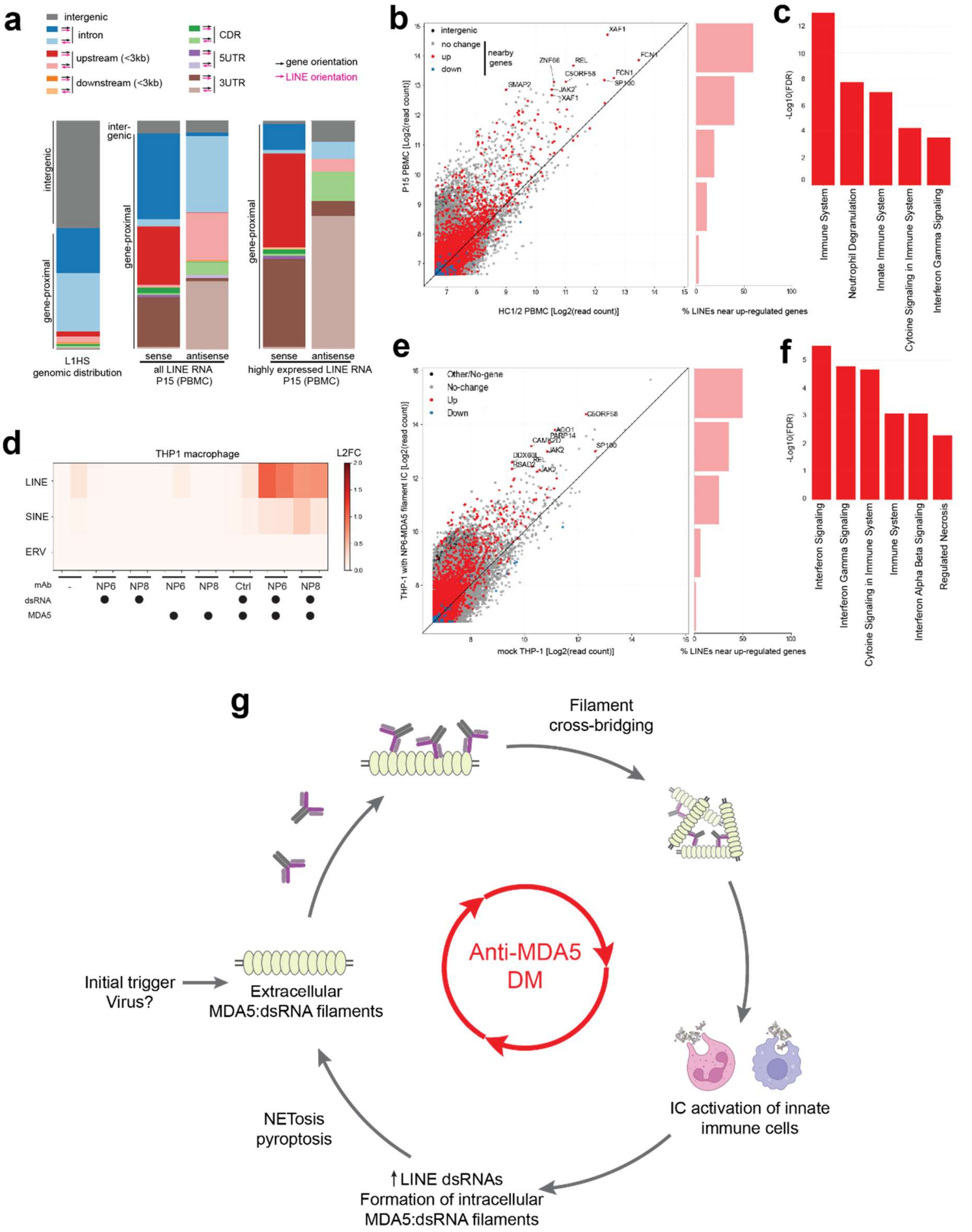

Figure 6. LINE-derived RNAs are induced by MDA5 immune complex stimulation.

a) Annotation of all L1HS regions in the genome (left), all LINE regions with uniquely mappable reads weighted with read counts (middle), and all LINE regions with over 200 uniquely mappable reads, weighted with read counts (right) in P15 PBMCs. Concordant orientation of LINE and gene (darker shading) generates sense LINE RNAs upon gene transcription, whereas discordant orientation (lighter shading) generates antisense LINE RNAs.

b) (Left) Scatterplot of spike-in-normalized read counts of individual LINE loci in P15 PBMC versus averaged read counts in HC1/2 PBMCs. Each point represents a LINE locus, grouped into those within 3 kb of an upregulated gene (L2FC > 0.3, red), a downregulated gene (L2FC < -0.3, blue), a gene with no change (|L2FC| ≤ 0.3, gray), or not within 3 kb of any gene (black). Only uniquely mappable reads were counted. (Right) Percentage of LINEs near upregulated genes in five bins.
c) Reactome pathway of genes nearby top 100 highly expressed and up-regulated LINEs in P15 PBMCs relative to HC1/2.
d) Heatmap of L2FC in expression of repeat elements in THP-1-derived macrophages stimulated with MDA5 monomer or filament ICs as in Figure 2a.
e) (Left) Scatterplot of reads-per-million (RPM) of individual LINE loci in THP-1 macrophages stimulated with NP6-MDA5 filament ICs versus mock control. Only uniquely mappable reads were counted. Each point is colored as in (b). (Right) Percentage of LINEs near upregulated genes in five bins.
f) Reactome pathway of genes nearby top 100 highly expressed and up-regulated LINEs in NP6-MDA5 filament IC-stimulated THP-1 relative to mock.
g) Model of MDA5 filament IC-mediated pathogenesis of anti-MDA5 DM. Extracellular MDA5 filaments released from cells undergo antibody-mediated aggregation. These complexes induce type I interferon signaling in innate immune cells, which upregulate expression of LINE RNA and MDA5 protein. LINE RNAs form double-stranded structures that scaffold cytoplasmic MDA5 filaments. These filaments are subsequently released extracellularly as innate immune cells activate inflammatory cell death programs like NETosis and pyroptosis. These events drive a self-amplifying feedforward loop of innate immune activation and inflammation, providing a mechanistic basis for the severe and often treatment-refractory inflammation in fulminant anti-MDA5 DM.

RNA-seq results contain 2 technical repeats for patient samples and 2 biological repeats for THP-1 data. L2FC, $\log_2$-fold change.

Extended Data Figures 1-10

Extended Data Tables 1-4

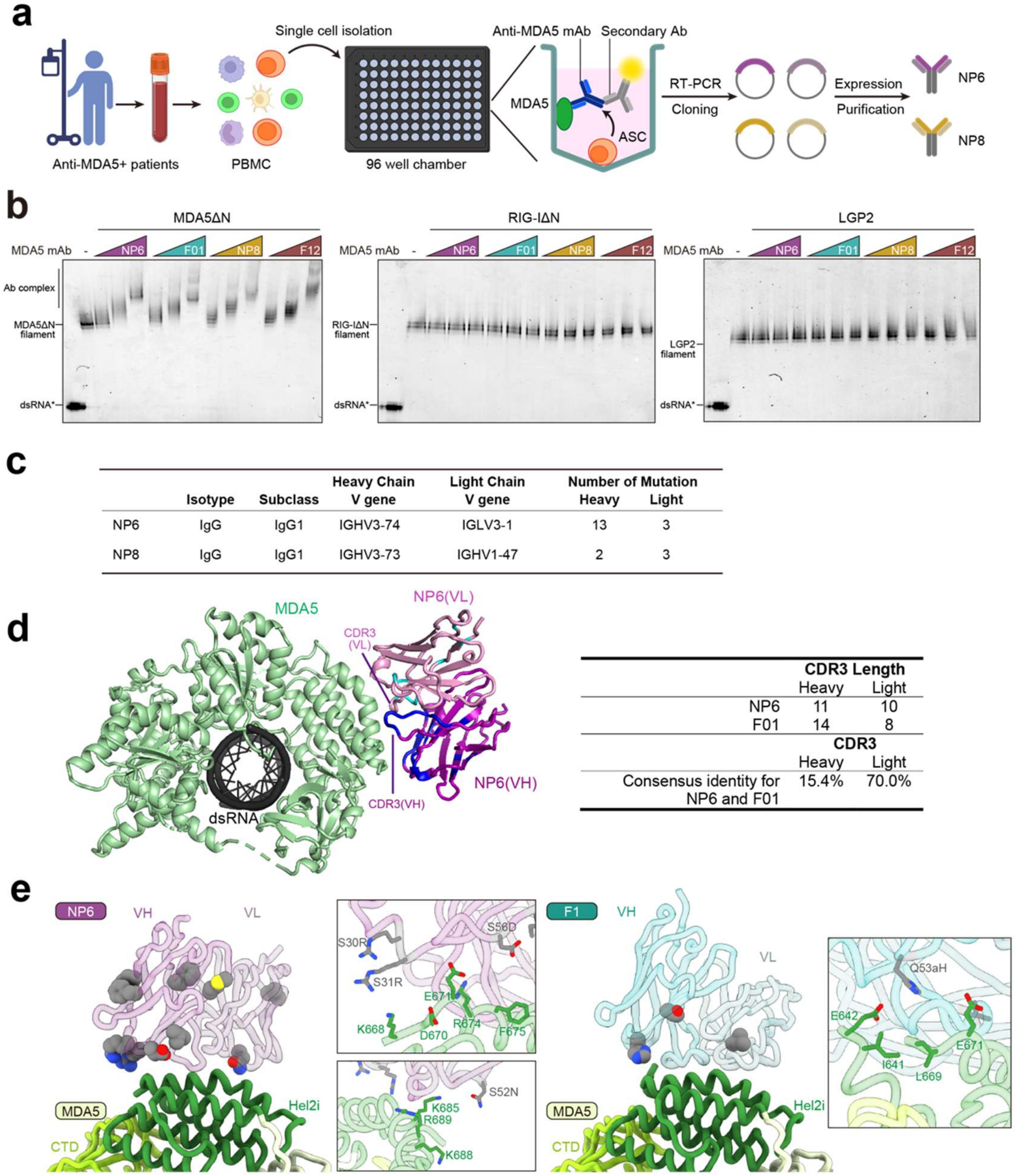

	Isotype	Subclass	Heavy Chain V gene	Light Chain V gene	Number of Mutation Heavy	Number of Mutation Light
NP6	IgG	IgG1	IGHV3-74	IGLV3-1	13	3
NP8	IgG	IgG1	IGHV3-73	IGHV1-47	2	3

	CDR3 Length Heavy	CDR3 Length Light
NP6	11	10
F01	14	8
	CDR3 Heavy	**CDR3** Light
Consensus identity for NP6 and F01	15.4%	70.0%

Extended Data Figure 1. B-cell cloning and sequences of monoclonal MDA5 antibodies

a) Schematic overview of the antibody cloning process of NP6 and NP8 from an anti-MDA5 DM patient. See Methods.
b) Native gel mobility shift assay showing specificity of MDA5 mAbs. RLR filaments were formed by mixing MDA5ΔN, RIG-IΔN, or LGP2 with Cy5-labeled (*) 112 bp dsRNA and incubated with MDA5 scFv. Anti-MDA5 scFv binds specifically to MDA5ΔN filaments but not RIG-I or LGP2.
c) Summary of NP6 and NP8 mAbs. Refer to Ref 24 for F01 and F12 mAbs.
d) Comparison of NP6 and F01. (Left) Structure of NP6 in complex with MDA5. Residues that differ from F01 are colored blue (heavy chain, VH) and cyan (light chain, VL). (Right) Comparison of CDR3 of heavy and light chains. Sequence identity was calculated using MAFFT alignment algorithm.

e) Mapping of somatic hypermutations (grey spheres) on NP6 (left) and F01 (right). Close-up views of boxed areas show that these mutated residues do not directly contact MDA5.

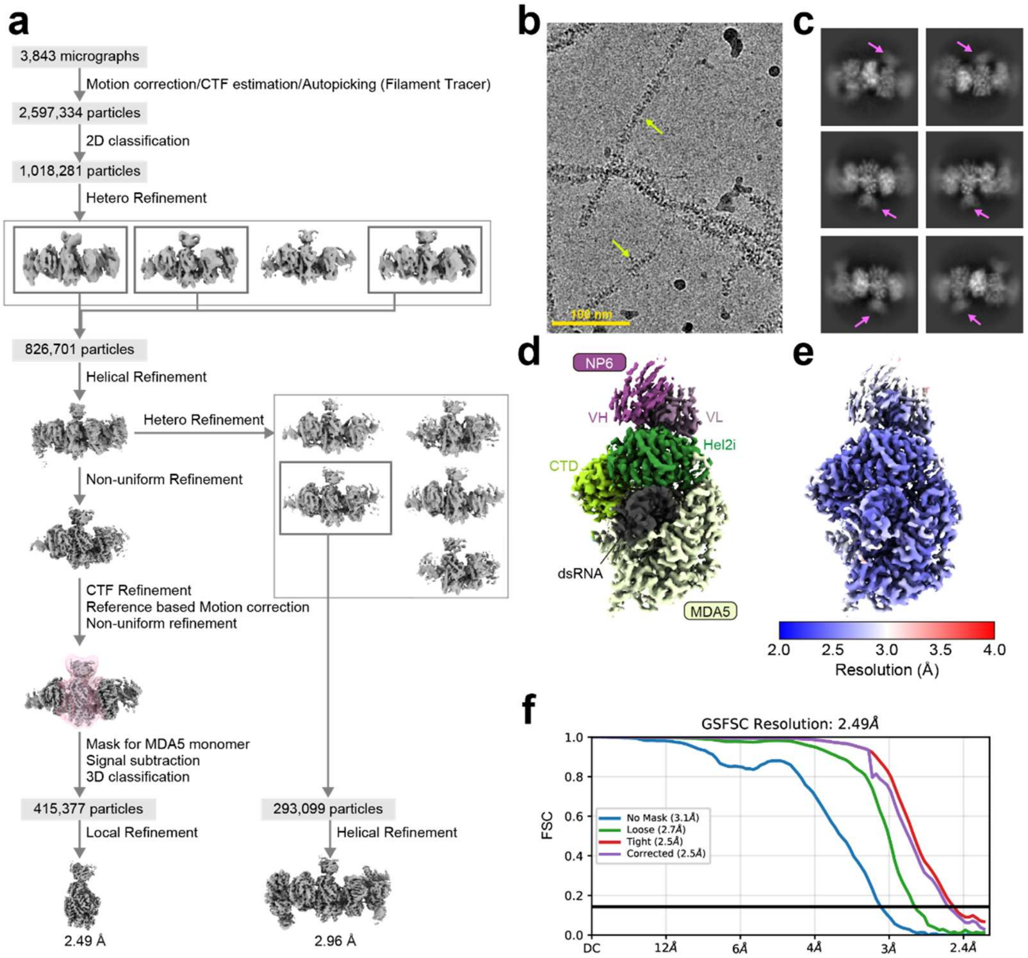

Extended Data Figure 2. Cryo-EM analysis of the MDA5ΔN:NP6 complex

a) Cryo-EM image processing workflow.
b) Representative cryo-EM micrograph at a magnification of 105,000x. The MDA5:dsRNA filaments are indicated by light green arrows.
c) Representative 2D class averaged images of particles used for the final reconstruction. The magenta arrows indicate NP6 antibody.
d) Cryo-EM density maps, colored according to the protein domains same as in Figure 1D.
e) Cryo-EM density maps, colored according to the local resolution.
f) Fourier shell correlation (FSC) curves calculated between the half-maps in the 3D reconstruction.

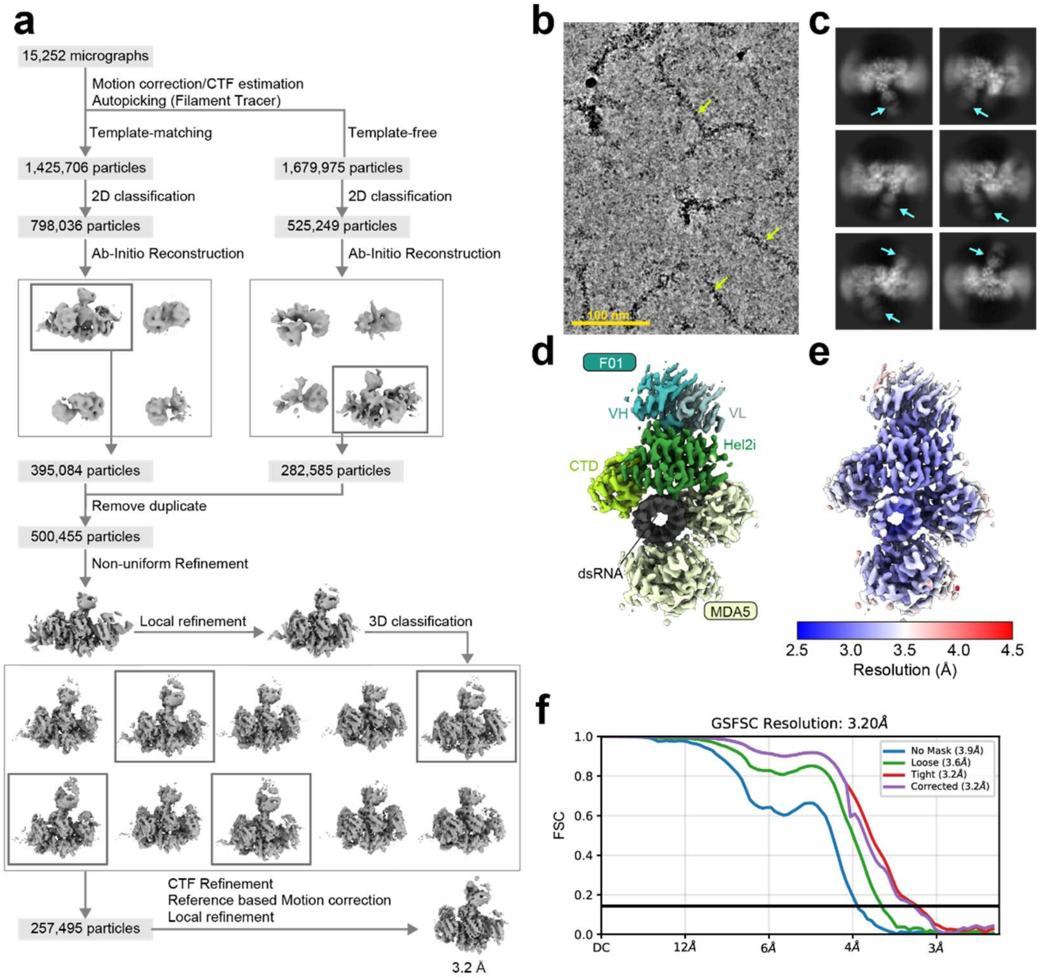

Extended Data Figure 3. Cryo-EM analysis of the MDA5ΔN:F01 complex

a) Cryo-EM image processing workflow.
b) Representative cryo-EM micrograph at a magnification of 105,000x. The MDA5:dsRNA filaments are indicated by light green arrows.
c) Representative 2D class averaged images of particles used for the final reconstruction. The cyan arrows indicate F01 anti-MDA5 antibody.
d) Cryo-EM density maps, colored according to the protein domains same as in Figure 1D.
e) Cryo-EM density maps, colored according to the local resolution.
f) Fourier shell correlation (FSC) curves calculated between the half-maps in the 3D reconstruction.

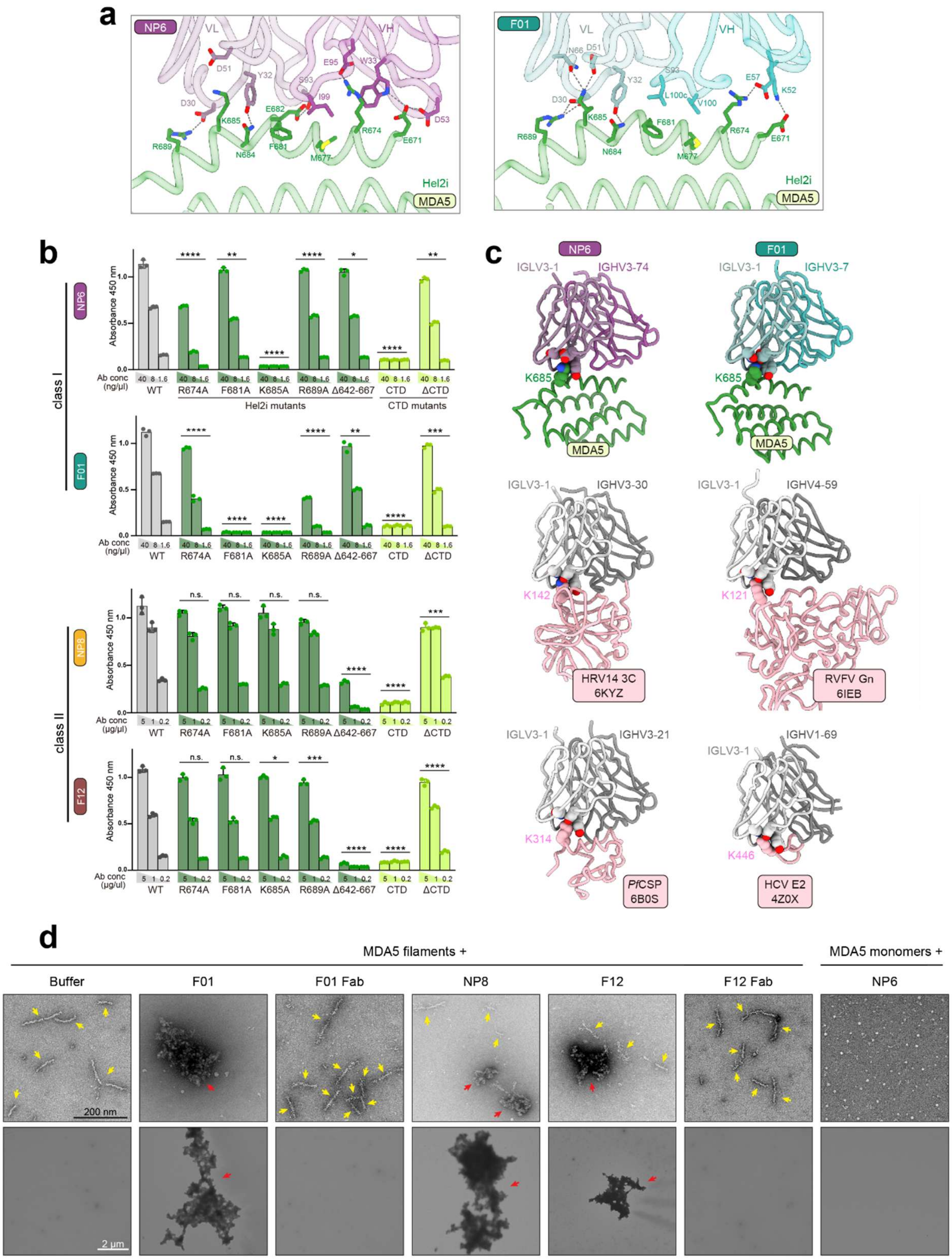

Extended Data Figure 4. Characterization and validation of MDA5–mAb interactions

a) Close-up view of the interaction between Hel2i domain of MDA5 and NP6 (left) or F01 (right). The residues involved in the interactions are shown as stick model.

b) Mutational analyses of MDA5-mAb interactions by ELISA. Monomeric WT MDA5ΔN and its variants were immobilized on ELISA plates and incubated with His-tagged scFv antibodies at three different concentrations. Antibodies bound to MDA5 were detected using an HRP-conjugated anti-His antibody. Data are presented as mean ± SD of 3 technical replicates. *P*-values were calculated by two-way ANOVA to compare antibody binding to WT versus mutant MDA5 across 3 Ab concentrations. **P* < 0.05, ***P* < 0.01, ****P* < 0.001, *****P* < 0.0001. *n.s*, not significant.

c) Conserved antigen–antibody interactions involving the IGLV3-1 light chain. Published structures are aligned to the light chain of NP6. The GRAB motif (Y32, D51, and N66) recognizes a conserved lysine residue.

d) (Top row) Negative stain images of MDA5 filaments formed by MDA5ΔN (G495R) (111 nM) ± 512 bp dsRNA (3.7 nM) bound by antibodies (27.8 nM), imaged at 25,000x magnification. (Bottom row) Filaments were formed with 2.7-fold higher protein and RNA concentrations and imaged at 2,000x. Yellow arrows indicate individual filaments, whereas red arrows indicate filament aggregates.

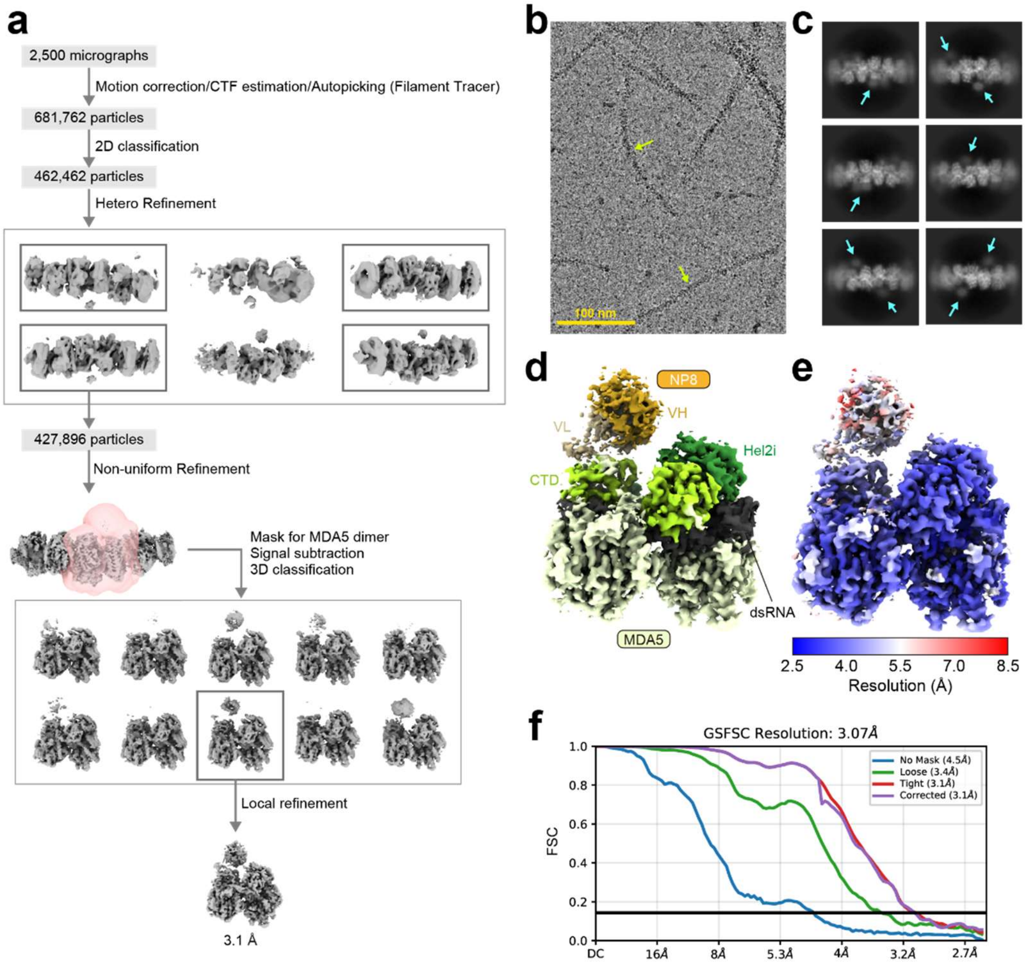

Extended Data Figure 5. Cryo-EM analysis of the MDA5ΔN:NP8 complex

a) Cryo-EM image processing workflow.
b) Representative cryo-EM micrograph at a magnification of 105,000x. The MDA5:dsRNA filaments are indicated by light green arrows.
c) Representative 2D class averaged images of particles used for the final reconstruction. The yellow arrows indicate NP8 anti-MDA5 antibody.
d) Cryo-EM density maps, colored according to the protein domains same as in Figure 1D.
e) Cryo-EM density maps, colored according to the local resolution.
f) Fourier shell correlation (FSC) curves calculated between the half-maps in the 3D reconstruction.

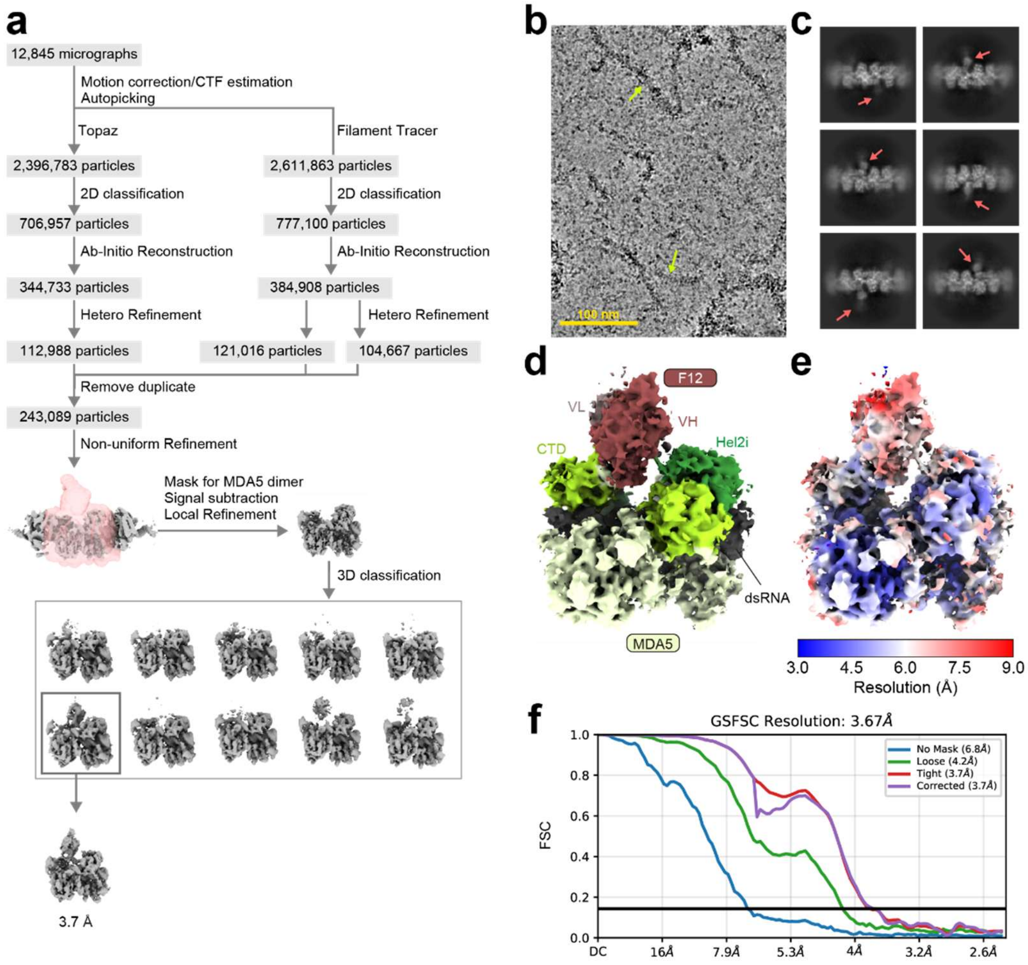

Extended Data Figure 6. Cryo-EM analysis of the MDA5ΔN:F12 complex.

a) Cryo-EM image processing workflow.

b) Representative cryo-EM micrograph at a magnification of 105,000x. The MDA5:dsRNA filaments are indicated by light green arrows.

c) Representative 2D class averaged images of particles used for the final reconstruction. The red arrows indicate F12 anti-MDA5 antibody.

d) Cryo-EM density maps, colored according to the protein domains same as in Figure 1D.

e) Cryo-EM density maps, colored according to the local resolution.

f) Fourier shell correlation (FSC) curves calculated between the half-maps in the 3D reconstruction.

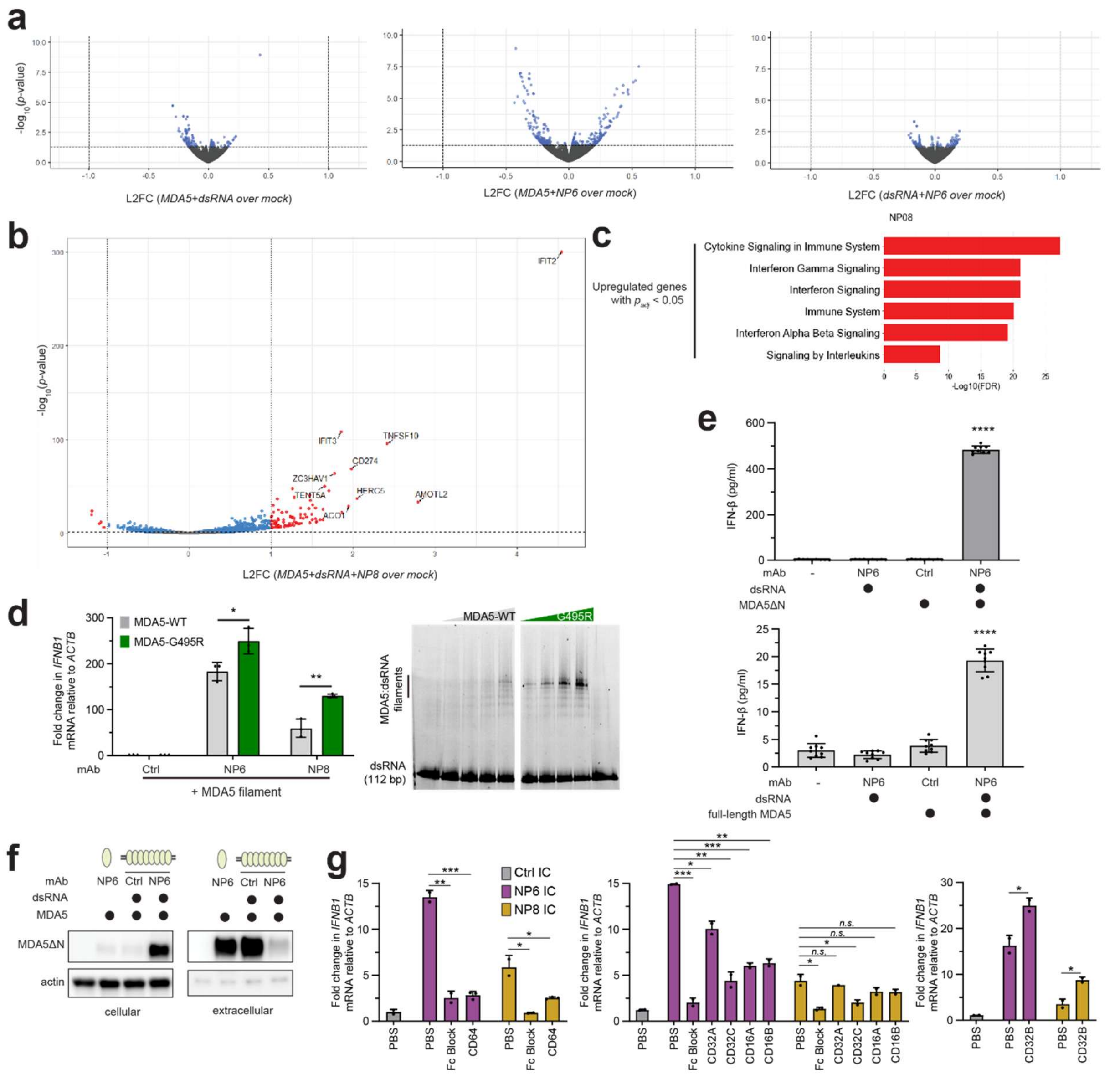

Extended Data Figure 7. MDA5 filament ICs activate inflammatory pathways in THP-1-derived macrophages

a) Volcano plots of THP-1-derived macrophages stimulated with MDA5ΔN filaments (90 nM; dsRNA 3 nM; left), MDA5 monomers (90 nM) with NP6 (90 nM) (middle), or dsRNA (3 nM) with NP6 (90 nM), relative to mock. Genes with log$_2$-fold change $|L2FC| > 1$ and $p < 0.05$ (red) are shown; all other genes shown have $p > 0.05$ (gray) or $p < 0.05$ (blue).

b) Volcano plot of differentially expressed genes in THP-1-derived macrophages stimulated with MDA5ΔN filament-NP8 ICs over mock. Each point is colored as in Figure 2a.

c) Reactome pathways of significantly upregulated genes in THP-1-derived macrophages stimulated with NP8-MDA5ΔN filament ICs over mock ($p_{adj} < 0.05$, L2FC > 0).

d) (Left) *IFNB1* mRNA levels in THP-1-derived macrophages stimulated with MDA5ΔN filaments formed by WT or gain-of-function G495R mutant (90 nM) and 512 bp dsRNA (3 nM), in complex with isotype control, NP6, or NP8 antibody (90 nM). Data was normalized to mock treatment. *P*-values were calculated by two-tailed Student's *t* test. (Right) Native gel mobility shift assay to monitor dsRNA binding capacity by MDA5. Filaments of MDA5ΔN-WT or -G495R (200-500 nM) were formed on 112 bp dsRNA (69 nM).

e) Secreted IFN-β levels measured by ELISA in THP-1-derived macrophages stimulated with either monomeric MDA5ΔN (upper) or MDA5 (lower) (90 nM) or dsRNA-bound filaments (90 nM; 512 bp dsRNA, 3 nM) in the presence of isotype control or NP6 antibody (90 nM). *P*-values were calculated by one-way ANOVA.

f) Cellular and extracellular MDA5ΔN protein levels in THP-1-derived macrophages stimulated with MDA5 monomer or filament ICs as in (e). 8 hours post-stimulation, supernatant and washed cell pellet were analyzed for MDA5ΔN, which was added extracellularly.

g) *IFNB1* mRNA levels in THP-1-derived macrophages pre-treated with PBS or FcγR antibodies (10 μg/ml) for 1.5 hours, then stimulated with dsRNA-bound MDA5ΔN filaments (13.5 nM; 512 bp dsRNA, 0.45 nM) and isotype control, NP6, or NP8 antibodies (13.5 nM). Data was normalized to mock treatment. *P*-values were calculated by two-tailed Student's *t* test.

Data are presented as mean ± SD of at least 2 biological replicates. RNA-seq results contain 2 biological repeats. All other data are representative of at least 3 independent experiments. **P* < 0.05, ***P* < 0.01, ****P* < 0.001, *****P* < 0.0001, *n.s.*, not significant.

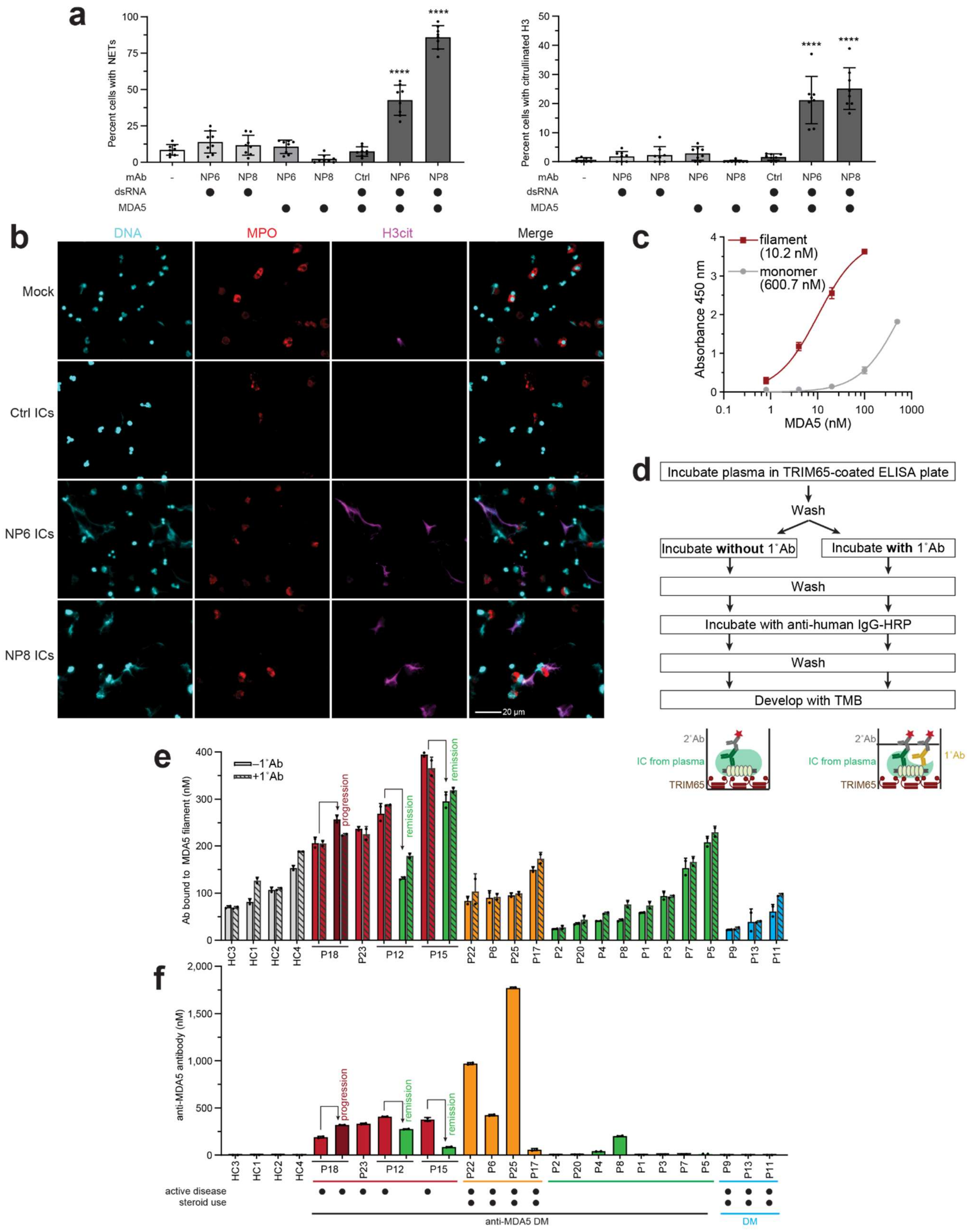

Extended Data Figure 8. Extracellular MDA5 filament ICs are present in anti-MDA5 DM and activate human neutrophils.

a) Quantitation of NETosis (left) and histone 3 citrullination (right) frequency in healthy human neutrophils stimulated with combinations of 512 bp dsRNA (3 nM), MDA5ΔN (90 nM), and/or isotype control or NP6/8 mAbs (20 nM). Four fields of view per well were analyzed from two biological replicates. Data are presented as mean ± SD. *P*-values were calculated by one-way ANOVA comparing relevant conditions for NP6 or NP8 ICs. ****$P < 0.0001$.

b) Immunofluorescence analysis of DNA (Hoechst 3342, cyan), myeloperoxidase (MPO, red), citrullinated histone 3 (H3cit, magenta) in healthy human neutrophils stimulated with MDA5ΔN filament ICs (MDA5ΔN, 90 nM; 512 bp dsRNA, 3 nM; mAb, 20nM). This experiment was repeated using neutrophils from three different healthy donors, which showed similar patterns (see Figure 3E).

c) Binding curves of TRIM65 to MDA5ΔN monomers or filaments, measured by sandwich ELISA, with apparent K_d shown in parentheses. Filaments were assembled from MDA5ΔN (5 μM) and 512 bp dsRNA (160 nM). Bound filaments were detected with F01 mAb (1˚) and anti-human IgG-HRP (2˚).

d) Workflow of TRIM65 sandwich ELISA in which TRIM65-captured MDA5ΔN filaments were incubated without NP8 to measure endogenous antibodies co-purified with MDA5 filament. This assay was repeated with the addition of 1˚ Ab (NP8), which would increase signal if additional antibody-binding sites on TRIM65-captured ICs remained available.

e) Plasma concentrations of antibodies bound to MDA5 filaments, determined by TRIM65 sandwich ELISA without or with NP8 probing. Addition of NP8 had minimal impact on signal, indicating that MDA5 filaments are largely saturated with endogenous antibodies. Antibody concentrations were interpolated from a standard curve generated using TRIM65-captured MDA5ΔN filaments (20 μM) assembled on 512 bp dsRNA (640 nM) and probed with NP8 (1˚Ab) followed by anti-human IgG-HRP (2˚Ab). Data are presented as mean ± SD of 2 technical replicates for 4 dilutions.

f) Plasma anti-MDA5 antibody concentrations determined by direct ELISA using MDA5ΔN-coated plates, calibrated using an NP6 standard curve. Data are presented as mean ± SD of 2 technical replicates for 4 dilutions. Active disease at the time of blood draw was defined by the treating physician and confirmed by a reviewing rheumatologist.

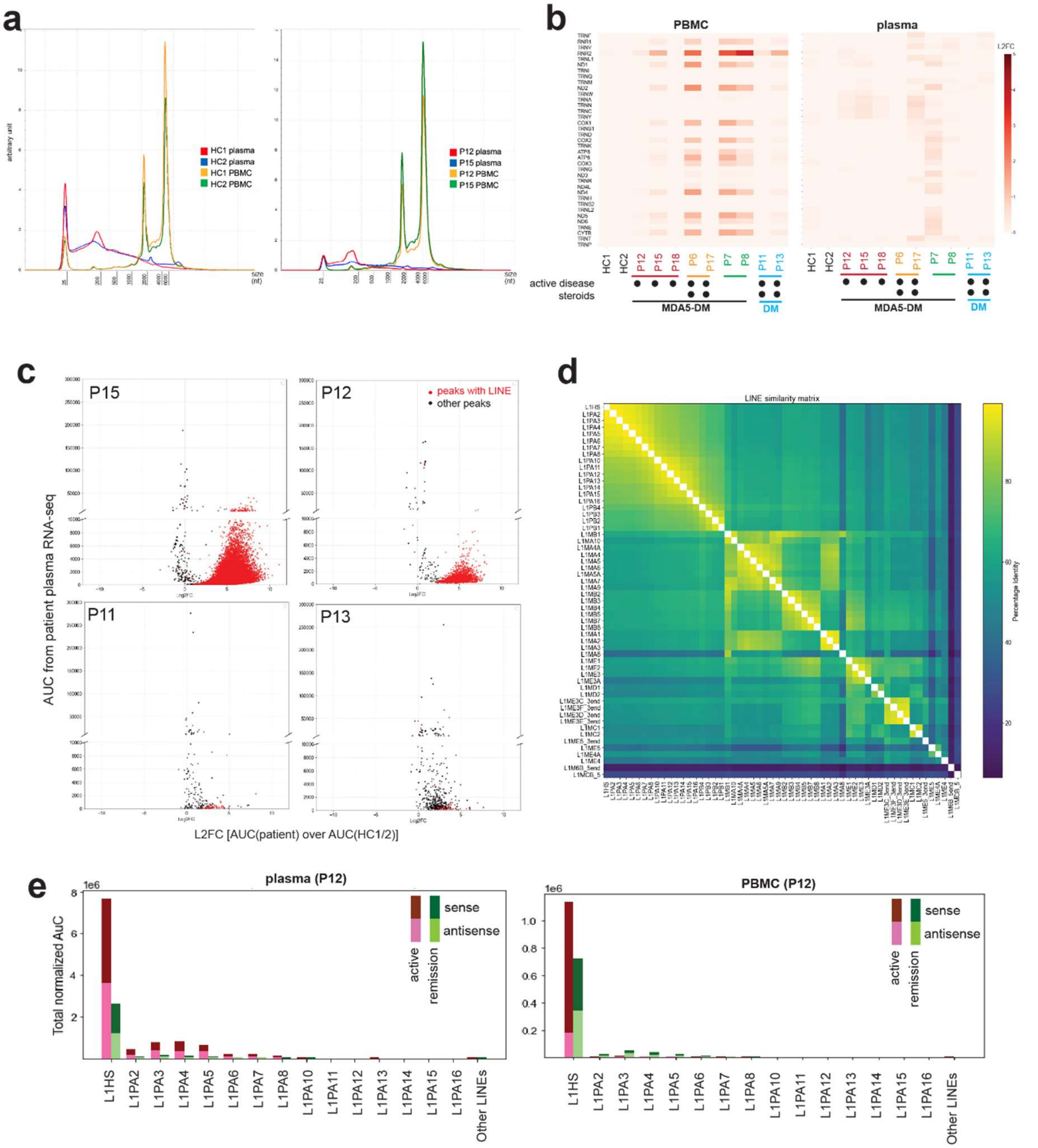

Extended Data Figure 9. LINE retroelements are enriched in anti-MDA5 DM plasma and PBMC RNA

a) Electropherogram of RNA extracted from plasma and PBMCs of healthy controls (left) and anti-MDA5 DM patients (right).
b) Heatmap of $\log_2$-fold change (L2FC) in mitochondrial RNAs in PBMCs (left) and plasma (right) of healthy controls and DM patients.
c) Whole genome peak calling and annotation of plasma RNA-seq from anti-MDA5 DM patients (P15, P12; top) and non-MDA5 DM patients (P11, P13; bottom). Peaks were called using HC1/2 plasma RNA-seq as the control. Each dot represents an individual peak, plotted by peak area under the curve (AUC) in patient samples (y-axis) versus L2FC in patients relative to healthy controls (x-axis). Peaks containing one or more LINE elements were colored red to distinguish from other peaks (black).

d) Similarity matrix of all LINE sequences based on Repbase, sorted by percentage identity value to L1HS.
e) Levels of LINE-1 (L1) and all other LINE elements in plasma (left) and PBMCs (right) from individual P12 during active (red) and quiescent (green) disease. Sense (dark) and antisense (light) sequences are shown.

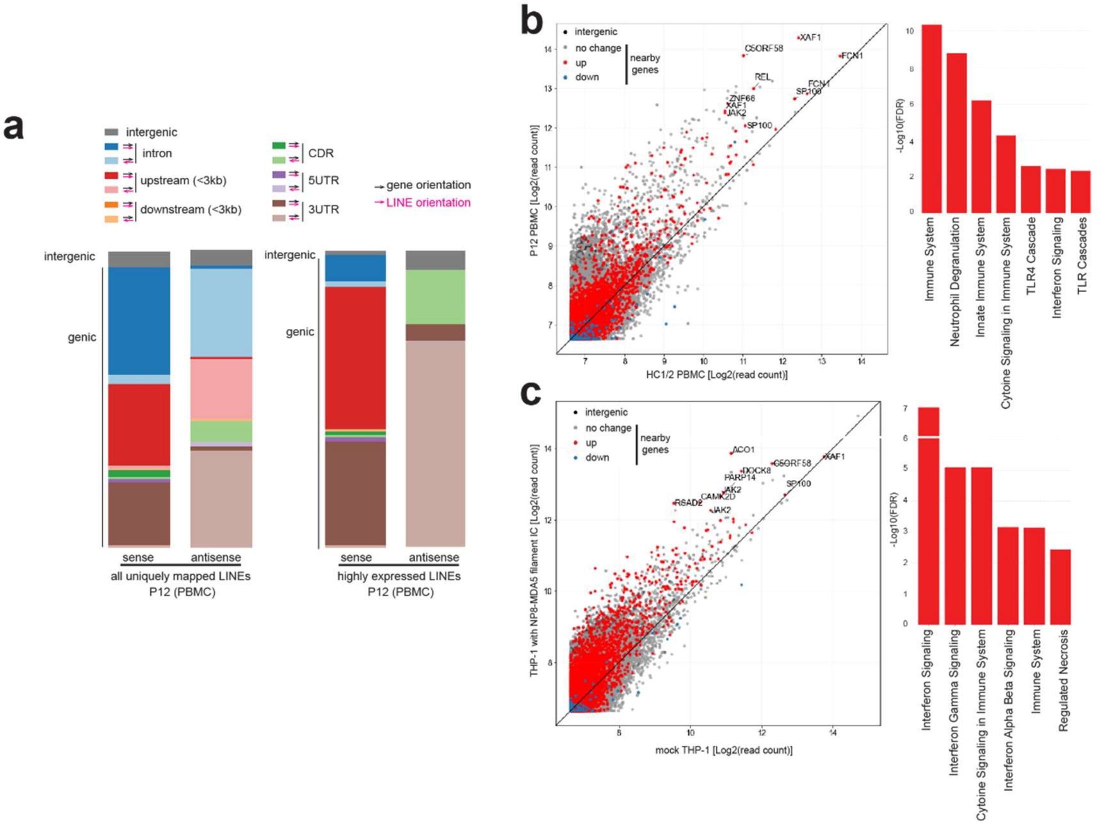

Extended Data Figure 10. MDA5 filament ICs induce the expression of LINEs in human PBMCs, macrophages, and neutrophils.

a) Annotation of all LINE regions with uniquely mappable reads weighted with read counts (left), and all LINE regions with over 200 uniquely mappable reads (right). Concordant orientation of LINE and gene (darker shading) generates sense LINE RNAs upon gene transcription, whereas discordant orientation (lighter shading) generates antisense LINE RNAs.

b) (Left) Scatterplot of spike-in-normalized read counts of individual LINE loci in P12 PBMC versus averaged read counts in HC1/2 PBMCs. Each point represents a LINE locus, grouped into those within 3 kb of an up-regulated gene (L2FC > 0.3, red), a down-regulated gene (L2FC < -0.3, blue), a gene with no change (|L2FC| ⩽ 0.3, gray), or not within 3 kb of any gene (black). (Right) Reactome pathway of genes nearby top 100 highly expressed and up-regulated LINEs in P12 PBMCs relative to HC1/2.

c) (Left) Scatterplot of reads-per-million (RPM) of individual LINE loci in THP-1 macrophage stimulated with NP8-MDA5 filament ICs versus mock control. Only uniquely mappable reads were counted. Each point is colored as in (b). (Right) Reactome pathway of genes nearby top 100 highly expressed and up-regulated LINEs in THP-1 stimulated with NP8-MDA5 filament ICs relative to mock control.

Basic demographics	
Age	55
Sex	Male
Cutaneous involvement	
Gottron's papules	Yes
Inverse Gottron's papules	Yes
Mechanic's hands	Yes
Ulcers	No
Facial and truncal erythema	Yes
Other involvement	
RP-ILD	Yes
Myositis	Yes
Laboratory findings	
Anti-MDA5 autoantibody, Index, (0-31)	4500
Anti-SS-A autoantibody, U/mL, (0-10)	25.6
Lymphocyte cout, /μL	645
KL-6 , U/mL, (0-464)	575
SP-D, ng/mL, (0-110)	26
Creatine kinase, U/L, (59-248)	1199
Aldolase, U/L , (2.7-7.5)	13.8
AST, U/L, (13-30)	142
ALT, U/L, (10-42)	90
CRP, mg/dL, (0-0.3)	0.94
ESR, mm/h, (2-10)	67
Ferritin, ng/mL, (14-304)	808
Disease activity score	
Physician's global disease activity (0-100)	78
Sampling	
Treatment at time of sampling	none
Sample type	Fresh PBMC

RP-ILD: Rapidly progressive interstitial lung disease
KL-6: Krebs von den Lungen-6
SP-D: surfactant protein-D
CRP: C-reactive protein

Extended Data Table 1. Characteristics of anti-MDA5 DM patient from whom antibody-secreting cells were isolated.

	MDA5-NP6 complex (EMDB-67964) (PDB 21SJ)	MDA5-NP8 complex (EMDB-68271)	MDA5-F01 complex (EMDB-68273) (PDB 22HM)	MDA5-F12 complex (EMDB-68272)
Data collection and processing				
Magnification	105,000	105,000	105,000	105,000
Voltage (kV)	300	300	300	300
Electron exposure (e–/Å^2)	50.0	50.0	59.6	60.00
Defocus range (μm)	−0.8 to −2.0	−0.8 to −2.0	−1.0 to −2.5	−0.8 to −2.5
Pixel size (Å)	0.83	0.83	0.83	0.827
Symmetry imposed	C1	C1	C1	C1
Initial particle images (no.)	2,597,334	681,762	3,105,681	2,396,783
Final particle images (no.)	415,377	41,489	257,495	25,448
Map resolution (Å)	2.49	3.07	3.20	3.67
FSC threshold	0.143	0.143	0.143	0.143
Refinement				
Model resolution (Å)	2.7		3.5	
FSC threshold	0.5		0.5	
Map sharpening *B* factor (Å^2)	86.1		127.6	
Model composition				
Non-hydrogen atoms	7691		7530	
Protein residues	883		862	
Nucleotide residues	30		30	
Ligands	2		2	
B factors (Å^2)				
Protein	44.52		92.19	
Ligand	50.90		125.11	
R.m.s. deviations				
Bond lengths (Å)	0.002		0.003	
Bond angles (°)	0.559		0.490	
Validation				
MolProbity score	1.32		1.45	
Clashscore	5.88		8.25	
Poor rotamers (%)	0		0.13	
Ramachandran plot				
Favored (%)	98.04		98.81	
Allowed (%)	1.96		1.19	
Disallowed (%)	0		0	

Extended Data Table 2. Cryo-EM data collection, refinement, and validation statistics.

	Dermatomyositis (*n* = 19)	Healthy (*n* = 4)
Demographics		
Mean age, years (SD)	54.7 (15.0)	27.8 (6.6)
Female, n (%)	15 (78.9)	3 (75.0)
Race, n (%)		
White	14 (73.7)	0 (0)
Non-white	5 (26.3)	4 (100)
Ethnicity, n (%)		
Hispanic	1 (5.3)	1 (25)
Disease history		
Disease duration (months), median (IQR)	21 (36.5)	NA
Immunosuppressive treatment, n (%)	19 (100)	NA
Anti-Jo-1, n (%)	0 (0)	NA
Anti-Mi-2, n (%)	2 (10.5)	NA
Anti-PL-7, n (%)	0 (0)	NA
Anti-PL-12, n (%)	0 (0)	NA
Anti-EJ, n (%)	0 (0)	NA
Anti-OJ, n (%)	0 (0)	NA
Anti-SRP, n (%)	0 (0)	NA
Anti-SAE, n (%)	0 (0)	NA
Anti-MDA5, n (%)	16 (84.2)	NA
Anti-NXP2, n (%)	0 (0)	NA
Anti-TIF1y, n (%)	3 (15.8)	NA
Anti-PM/Scl, n (%)	0 (0)	NA
Anti-SS-A, n (%)	5 (26.3)	NA
Anti-Ku, n (%)	0 (0)	NA
Anti-U1RNP, n (%)	0 (0)	NA

Extended Data Table 3. Demographic and clinical characteristics of dermatomyositis cohort used to characterize extracellular MDA5 filament immune complexes.
NA, not applicable.

	Anti-MDA5-positive Active disease (*n* = 8)	Anti-MDA5-positive Inactive disease (*n* = 8)	Anti-MDA5-negative Active disease (*n* = 3)
Clinical findings			
Muscle weakness, n (%)	0 (0)	0 (0)	3 (100)
Elevated muscle enzymes, n (%)	1 (12.5)	0 (0)	2 (66.7)
Heliotrope rash, n (%)	1 (12.5)	0 (0)	2 (66.7)
Gottron's papules, n (%)	5 (62.5)	1 (12.5)	3 (100)
ILD, n (%)	8 (100)	8 (100)	0 (0)
Subclinical, n (%)	1 (12.5)	0 (0)	NA
Mild, n (%)	5 (62.5)	5 (62.5)	NA
Moderate, n (%)	0 (0)	2 (25)	NA
Severe, n (%)	2 (25)	1 (12.5)	NA
RP-ILD, n (%)	0 (0)	0 (0)	NA
Arthritis, n (%)	3 (37.5)	0 (0)	0 (0)
Dermatomyositis disease activity			
Low disease activity or remission, n (%)	0 (0)	8 (100)	0 (0)
Moderate or high disease activity, n (%)	8 (100)	0 (0)	3 (100)
Immunomodulating or immunosuppressing treatment			
Hydroxychloroquine, n (%)	0 (0)	0 (0)	1 (33.3)
Intravenous immunoglobulin, n (%)	3 (37.5)	5 (62.5)	0 (0)
CD20 inhibitor, n (%)	1 (12.5)	1 (12.5)	0 (0)
Abatacept, n (%)	0 (0)	1 (12.5)	0 (0)
JAK inhibitor, n (%)	1 (12.5)	0 (0)	0 (0)
Methotrexate, n (%)	2 (25)	0 (0)	1 (33.3)
Leflunomide, n (%)	0 (0)	0 (0)	0 (0)
Mycophenolate mofetil, n (%)	1 (12.5)	5 (62.5)	0 (0)
Azathioprine, n (%)	0 (0)	0 (0)	0 (0)
Calcineurin inhibitor, n (%)	1 (12.5)	1 (12.5)	0 (0)
Systemic glucocorticoids, n (%)	4 (50)	0 (0)	3 (100)
Prednisone-equivalent daily dose (median, IQR, mg)	50 (34.1)	NA	60 (0)

Extended Data Table 4. Clinical characteristics of participants based on anti-MDA5 positivity and disease activity at time of sample collection.
ILD: interstitial lung disease; RP-ILD, rapidly progressive interstitial lung disease; NA, not applicable.

Methods

Material Preparation

Cell Lines. THP-1 cells (gift from Dr. J. Kagan, Harvard Medical School) were maintained in RPMI-1640 (GE Healthcare) supplemented with 10% heat-inactivated fetal bovine serum. Cells were grown at 37°C in a 5% CO_2 humidified atmosphere. Cells were routinely tested for mycoplasma contamination.

Protein expression and purification. MDA5 and LGP2 proteins were expressed in Sf9 cells using the Bac-to-Bac baculovirus expression systems (Thermo Fischer Scientific). Sf9 cells were infected in Sf-900 culture media (Thermo Fischer Scientific) for 48-60 h at 27°C. Cells were harvested, lysed by sonication, and clarified by centrifugation. The supernatant was applied to Ni-NTA agarose (QIAGEN) and the eluted protein was treated with HRV 3C protease at 4°C overnight to cleave the N-terminal tag. The proteins were further purified by affinity chromatography using a HiTrap Heparin column (Cytiva), followed by size-exclusion chromatography on a Superdex 200 Increase 10/300 column (Cytiva).

MDA5ΔN and RIG-IΔN proteins were expressed in *Escherichia coli* Rosetta2 (DE3) (Novagen) by induction with 0.25 mM isopropyl β-D-thiogalactopyranoside (IPTG) at 18°C overnight. Cells were lysed by sonication and clarified by centrifugation. N-terminally His_6-SUMO-tagged MDA5ΔN, RIG-IΔN, and its variants were purified using Ni–NTA agarose chromatography. The eluted proteins were incubated with Ulp1 protease at 4°C for 4 h to cleave the His_6-SUMO-tag. The proteins were further purified by chromatography on HiTrap Heparin and Superdex 200 Increase 10/300 columns.

$TRIM65^{CC\text{-}PSpry}$ (residues 125-517) protein expression and lysis were done in the same manner as MDA5 and LGP2 in Sf9 cells, while protein purification was done by chromatography on Strep-Tactin Superflow (IBA). The eluted protein was treated with HRV 3C protease, and further purified by size-exclusion chromatography on Superdex 200 Increase 10/300 columns.

All MDA5 antibodies were expressed in Expi293 cells (Thermo Fischer Scientific). Culture supernatants were collected by centrifugation 5 days post-transfection. IgG antibodies were purified using a rProteinA column (Cytiva), followed by size-exclusion chromatography on Superdex 200 Increase 10/300 column. scFv of MDA5 antibodies were purified using Ni-Sepharose Excel column (Cytiva) and Superdex 200 Increase 10/300 column. Fab fragments of MDA5 antibodies were prepared with papain digestion at 1 mg/mL IgG and IgG:papain mass ratio of 20:1 in PBS with 10 mM EDTA and 10 mM L-Cysteine at 37°C for 1 hour. Digestion was quenched with 50 mM iodoacetamide. After buffer exchange with 50 mM Tris-HCl (pH 7), Fabs were purified with anion exchange chromatography (1 ml HiTrap SP FF, GE Healthcare) at 1 mL/min flow rate in Tris-HCl (pH 7) with a gradient in the same buffer to 1 M NaCl in 30 ml.

All purified proteins were flash-frozen in liquid nitrogen and stored at –80°C until use. All proteins used in cell-based experiments were tested for endotoxins at < 0.1 EU/mL using a chromogenic endotoxin quant kit (Pierce).

RNA preparation. dsRNAs were prepared by in vitro T7 transcription as previously described[1]. The sequences of 112, 162, 512, and 1012 bp dsRNAs were taken from the first 100, 150, 500, and 1000 bp of the MDA5 gene flanked by 5’-gggaga and 5’-tctccc, respectively. The two complementary strands were co-transcribed, and the duplex was separated from unannealed ssRNAs by 10% acrylamide gel electrophoresis in TBE buffer. RNA was gel-extracted using the Elutrap electroelution kit (Whatman), ethanol precipitated, and stored in 20 mM HEPES, pH 7.0

Collection of patient samples

For anti-MDA5 antibody cloning to generate NP6 and NP8, as outlined in Extended Data Figure 1a, peripheral blood mononuclear cells (PBMCs) and plasma were collected from a Japanese patient with positive anti–MDA5 antibody (by clinical ELISA testing) and rapidly progressive interstitial lung disease (RP-ILD) prior to treatment. The patient met the Sontheimer criteria for clinically amyopathic dermatomyositis (CADM)[2]. The study was conducted in accordance with the Declaration of Helsinki and was approved by the Ethics Committee of the University of Tokyo Graduate School of Medicine. Written informed consent was obtained from all participants.

For anti-MDA5 antibody cloning to generate F01 and F12, PBMCs and sera were collected from 3 anti-MDA5-positive patients diagnosed between 1999 and 2021 at Karolinska University Hospital (Stockholm, Sweden), as reported separately[3].

PBMCs and plasma samples for Figures 4-6 were collected between March 2022 and December 2025 from patients diagnosed with dermatomyositis (DM) at Brigham and Women's Hospital (Boston, USA). Dermatomyositis diagnosis was made in accordance with EULAR/ACR criteria[4] and clinical designation of anti-MDA5-positivity was determined by clinical testing by the Oklahoma Medical Research Foundation Myositis profile. The study was performed with informed consent in accordance with protocols approved by the Mass General Brigham Institutional Review Board. Clinical variables of interest regarding the DM diagnosis were extracted from the electronic health record by manual chart review. These included the subject's age, sex, race, ethnicity, DM duration, autoantibody status, presence of muscle weakness, DM skin findings, ILD severity, inflammatory arthritis, and DM immunomodulatory medications (including the specific dose of any glucocorticoid when applicable). CK and aldolase were measured using commercial assays in the clinical laboratory at Brigham and Women's Hospital. Disease activity level was determined by the global assessment from the last rheumatology provider note documented in the electronic health record. ILD severity was graded based upon fulfillment of the following parameters: subclinical, undiagnosed or asymptomatic with <5% involvement on CT; mild, minimally symptomatic but not requiring treatment, may have seen a pulmonologist but does not require frequent management with <10% involvement on CT; moderate, symptomatic and on treatment requiring regular pulmonology follow up with >10% involvement on CT; and severe, symptomatic and on treatment, with regular pulmonology follow up, on supplemental oxygen or with flares requiring hospitalization or treatment escalation.

Isolation of human plasma, PBMCs, and neutrophils

Plasma and PBMCs were isolated from the same anticoagulated whole-blood sample collected in EDTA tubes. Whole blood was centrifuged at 1,500 x *g* for 10 minutes at RT (RT), and the plasma supernatant was carefully collected and stored at −80°C until further analysis. The remaining cellular fraction was diluted 1:1 with phosphate-buffered saline (PBS) and layered onto a Lymphoprep Tube (Abbott Diagnostics Technologies

AS, Oslo, Norway) or Ficoll-Paque (Cytiva). Density-gradient centrifugation was performed at 800 x *g* for 30 minutes at RT with the brake disengaged. The PBMC layer at the plasma–gradient interface was collected, washed twice with PBS (250 x *g* for 10 minutes), treated with 1x RBC lysis buffer (Invitrogen), and resuspended for downstream immunological assays. Cell number and viability were assessed using trypan blue exclusion.

Neutrophils were collected from 3 mL of peripheral blood collected from healthy controls in EDTA tubes. Neutrophils were isolated using Histopaque-1119 (Sigma) and Percoll Plus (GE Healthcare) gradients as described previously[5], which is a method that causes minimal activation of neutrophils during isolation. Purity of cells was >95% as determined by Wright-Giemsa staining.

Generation of patient-derived NP6 and NP8 mAbs

Single-cell isolation of anti-MDA5 antibody secreting cells. PBMC (1 x 10^6 cells) obtained from an anti-MDA5 antibody-positive CADM patient were loaded onto microchambers[6] (20 μm in diameter; 196,000 microwell array on a chip) that had been pre-coated with 5 μg/mL MDA5 antigen. Single-cell analysis was performed using an automated single-cell analysis and isolation system, which enables high-throughput screening with a microchamber array–based single-cell picking platform (AS ONE, Osaka, Japan). Antibody secretion from individual cells was assessed using an on-chip fluorescence immunoassay with an Alexa Fluor 488–conjugated goat anti-human IgG antibody (Invitrogen, A11013). Cells exhibiting high fluorescence intensity were identified as anti–MDA5 antibody–secreting cells. These cells were individually collected using a glass capillary attached to an automated micromanipulator and transferred into tubes containing cell lysis buffer for subsequent analyses.

VH and VL sequencing. Complementary DNA (cDNA) from each single anti–MDA5 antibody–producing cell was synthesized and amplified using SuperScript IV Single Cell/Low-Input cDNA PreAmp Kit (Thermo Fisher Scientific (ThermoFisher), according to the manufacturer's instructions.

Primary and secondary polymerase chain reaction (PCR) amplifications of the immunoglobulin heavy-chain variable region (VH) and light-chain variable region (VL) were performed using a universal forward primer and gene-specific reverse primers, as previously described[7,8]. Products from the secondary PCR were separated on a 1% agarose gel prepared in TAE buffer. Amplified VH and VL DNA fragments of approximately 600–750 base pairs were excised from the gel and purified using the PCR Clean-Up and Gel Extraction Kit (Takara, 740609). The purified VH and VL DNA fragments were cloned into the pGEM-T Easy vector (Promega, A1360) and subjected to Sanger sequencing.

Generation of patient-derived F01 and F12 mAbs

For generation of monoclonal anti-MDA5 antibodies F01 and F12, PBMCs were isolated from 3 anti-MDA5-positive patients diagnosed between 1999 and 2021 at Karolinska University Hospital (Stockholm, Sweden), and isolation of MDA5-specific B cells and sequencing of monoclonal BCRs are described separately[3].

Enzyme-linked immunosorbent assay (ELISA)

Anti-MDA5 sandwich ELISA. 96-well polystyrene high bind microplate for ELISA (Corning) was incubated with or without anti-MDA5 antibodies (1 µg/mL in PBS) overnight at 4ºC. The wells were then blocked with blocking buffer (5% BSA in PBS-T) for 2 h at RT. After blocking, the plates were incubated with FLAG-MDA5ΔN:512 bp dsRNA (0.3 nM to 4.0 µM) in blocking buffer for 1.5 h at RT. Plates were then washed with PBS-T three times, then incubated with anti-FLAG M2-peroxidase (HRP) at a dilution of 1:10,000 in blocking buffer for 1 h. Plates were washed with PBS-T three times. Plates were developed using TMB (Thermo Fisher Scientific) for 2-3 min, and the reaction was stopped by adding 1 M hydrochloric acid. Absorbance at 450 nM was measured using a Biotek M1 Synergy microplate reader within 30 min of stopping the reaction. Signal arising from uncoated wells were subtracted from antibody-coated wells.

Direct MDA5 ELISA. MDA5 and its variants (2-5 µg/ml) were coated onto 96-well Nunc MaxiSorp ELISA plates (Thermo Fisher Scientific) and incubated for 2 h at RT. The wells were then blocked with blocking buffer (5% BSA in TBS-T) for 1 h at RT. After blocking, the plates were washed three times with TBS-T. The scFv-formatted MDA5 antibodies were added and incubated at RT for 1 h, followed by three washes with TBS-T. For detection, a secondary antibody (HRP-conjugated mouse anti-His-tag; MBL) was diluted 1:5,000 in blocking buffer, added to each well, and incubated for 30 min. The plates were washed three times with TBS-T and then incubated with ELISA POD Substrate Solution (Nacalai Tesque) for 2-3 min. The reaction was stopped by adding 1 N sulfuric acid Stop Solution (Nacalai Tesque). Absorbance at 450 nm was measured using a SpectraMax iD5e plate reader (Molecular Devices) within 30 min of stopping the reaction.

For patient anti-MDA5 autoantibody detection, high bind ELISA microplates (Corning) were coated with or without MDA5ΔN (2 µg/ml in PBS with 2 mM DTT) overnight at 4°C. The wells were blocked with blocking buffer (5% BSA in PBS-T) for 2 h at RT, then washed with PBS-T three times. The plate was incubated with NP6 mAb 0.128 ng/mL to 10 µg/mL for standard curve) or human plasma diluted at 1:10 to 1:10,000 in plasma dilution buffer (1 mg/mL nuclease-free BSA in PBS) for 1 h. The plate was washed three times, then incubated with anti-human IgG-HRP (Promega) at 1:5,000 in blocking buffer for 1 h. Plates were washed with PBS-T three times and developed as described above for anti-MDA5 sandwich ELISAs.

IFN-β and IL-1β ELISAs. THP-1 cells were seeded into 48-well plates at a density of 1 x 10^6/mL. Cells were stimulated with ICs composed of MDA5ΔN (90 nM), 512 bp dsRNA (3 nM), and mAb (90 nM), or otherwise indicated in the text. At 4 hours post-stimulation, supernatant was harvested and used for ELISA. For IFN-β ELISA, the LumiKine Xpress hIFN-b 2.0 kit (InvivoGen) was used according to the manufacturer’s instructions; similarly, IL-1b ELISA was performed with the Human Il-1 beta/IL-1F2 ELISA kit Quantikine kit (R&D Systems) was used.

TRIM65 sandwich ELISA. 96-well polystyrene high bind microplate for ELISA (Corning) was incubated with or without TRIM65$^{\text{CC-PSpry}}$ (1 µg/mL in PBS with 2 mM DTT) overnight at 4ºC. The wells were blocked with blocking buffer (5% BSA in PBS-T) for 3 h at RT. After blocking, the plates were incubated with MDA5ΔN:512 bp dsRNA (4 to 100 nM for standard curve) or human plasma diluted at 1:50, 1:75, 1:100, 1:150, 1:200 in plasma dilution buffer for 1.5 h at RT. Plates were then washed with PBS-T three times, then incubated with anti-human IgG-HRP (Promega) at 1:5,000 in blocking buffer for 1 h. Plates were washed with PBS-T three times and developed as described above for anti-MDA5 sandwich ELISAs.

Native gel-shift assay

Assays were performed as previously reported[1]. For demonstration of mAb binding to RLR proteins, purified MDA5ΔN, RIG-IΔN, or LGP2 proteins were incubated with Cy5-labeled 112-bp dsRNA for 20 min at RT in binding buffer containing 20 mM HEPES (pH 7.5), 100 mM NaCl, 1.5 mM $MgCl_2$ and 2 mM ATP. Subsequently, scFv MDA5 antibodies were added, and the mixtures were further incubated at RT for 10 min. Samples were then analyzed on Bis-Tris native PAGE (Life Technologies). Gels were imaged by detecting Cy5 fluorescence using an iBright FL1500 imaging system (Thermo Fisher Scientific). For demonstration of differential dsRNA binding by MDA5 WT or gain-of-function mutant, purified MDA5ΔN-WT or -G495R proteins (200-500 nM) were incubated with 112-bp dsRNA (5 ng/µL) for 15 min at RT in the same binding buffer. The complex was analyzed on Bis-Tris native PAGE after staining with SybrGold stain (Life Technologies). SybrGold fluorescence was recorded using the iBright FL1500 imaging system.

Negative-stain electron microscopy

MDA5ΔN-G495R (111 nM) was incubated with 512 bp dsRNA (3.7 nM) in 20 mM HEPES pH 7.5, 100 mM NaCl, 1.5 mM MgCl2, and incubated at RT for 15 min, followed by addition of 1 mM $ADP·AlF_x$. $ADP·AlF_x$ was prepared by mixing ADP, $AlCl_3$, and NaF in a molar ratio of 1:1:3. Antibodies were added (27.8 nM) and incubated at RT for an additional 5 min. Samples were then adsorbed to carbon-coated grids (Electron Microscopy Sciences) and stained with 0.75% uranyl formate as described[9]. Images were collected using the JEM-1400 transmission electron microscope (JEOL) at a magnification of 300x to 25,000x.

Strep-Tactin pull-down assay

Twin-Strep-tagged or untagged MDA5ΔN (0.5 µM) was mixed with either 112 bp (bait) or 162 bp (prey) double-stranded RNA (dsRNA) at a concentration of 1 ng/µl and incubated at RT for 20 min in binding buffer containing 20 mM HEPES pH 7.5, 150 mM NaCl, and 1.5 mM $MgCl_2$. The resulting bait filaments were captured using MagStrep Strep-Tactin XT beads (IBA Lifesciences). Beads were washed three times with the same buffer to remove unbound bait filaments, followed by the addition of prey filaments together with either NP6 or NP8 antibodies. Bound dsRNAs were eluted by treatment with Proteinase K (160 U/ml) and analyzed by 4–16% Bis–Tris native polyacrylamide gel electrophoresis (PAGE) (Life Technologies). Gels were stained with SybrGold and imaged using an iBright FL1500 imaging system.

Cryo-EM sample preparation and data collection

For the complex with NP6 and NP8, scFv format of MDA5 antibodies was used. Purified MDA5ΔN G495R (1 mg/mL) was incubated with the 1012 bp dsRNA (0.050 mg/mL) in 50 mM HEPES, pH 7.5, 100 mM NaCl, 10 mM $MgCl_2$ at RT for 20 min. The mixture was then incubated with anti-MDA5 scFv at 1:1.2 molar ratio relative to MDA5ΔN at 4°C until cryo-EM grid preparation. The complex was further incubated in the presence of 2 mM ADP at 4°C for 10 min just before grid preparation. The samples (3 µL) were applied to a freshly glow-discharged Au 300 mesh R1.2/1.3 grid (Quantifoil), in a Vitrobot Mark IV (FEI) at 4°C with a blotting time of 4 seconds under 100% humidity conditions. The grid was plunge-frozen in liquid ethane cooled at liquid nitrogen temperature. The cryo-EM data were collected using a Titan Krios microscope (Thermo Fisher Scientific) installed at the University of Tokyo, running at 300 kV and equipped with a Gatan Quantum-LS Energy Filter (GIF) and a Gatan K3 Summit direct electron detector, operated in the electron counting mode. Movies were recorded at a nominal magnification of 105,000x, corresponding to a calibrated pixel size of 0.83 Å. The electron flux was set to 7.31 e−/pix/sec for 4.83 seconds, resulting in accumulated exposures of 50.0 e−/Å^2. The data were automatically acquired using the EPU software (Thermo Fisher Scientific), with a defocus range of −0.8 to −2.0 µm, and 3,843 and 2,500 movies were obtained for NP6 and NP8, respectively.

For the complex with F01 and F12, Fab fragments were used. Purified MDA5ΔN G495R (9 µM) was incubated with 512 bp dsRNA (0.050 mg/mL) in 20 mM HEPES, pH 7.5, 100 mM NaCl, 1.5 mM $MgCl_2$ on ice for 1 h. The mixture was then incubated with anti-MDA5 Fabs at 1:1.3 molar ratio relative to MDA5ΔN on ice until cryo-EM grid preparation. F01 complex was then incubated in the presence of 2 mM ADP for a minimum of 20 min and 0.1% glutaraldehyde for a maximum of 10 min on ice. F12 complex was incubated with 2 mM ADP·AlF_x for a minimum of 20 min on ice just before grid preparation. The samples were applied to a freshly glow-discharged Au 200 mesh R1.2/1.3 grid in a Vitrobot Mark IV at 4°C with a blotting time of 7 seconds under 100% humidity conditions at the Harvard Cryo-EM Center for Structural Biology. The grid was plunge-frozen in liquid ethane cooled at liquid nitrogen temperature. The cryo-EM data was collected using a Titan Krios microscope (Thermo Fisher Scientific), running at 300 kV and equipped with a Gatan Quantum-LS Energy Filter (GIF) and a Gatan K3 Summit direct electron detector, operated in the electron counting mode. F01 complex dataset was collected at the UMass Chan Medical School Cryo-EM core, and F12 complex dataset at the Cryo-EM Facility at Janelia Research Campus at HHMI Institute. Movies were recorded at a nominal magnification of 105,000x, corresponding to a calibrated pixel size of 0.83 Å. The data were automatically acquired using the EPU software (Thermo Fisher Scientific), with a defocus range of −1.0 to -2.5 µm for F01 and -0.8 to -2.5 for F12. 15,252 and 12,845 movies were obtained for F01 and F12, respectively.

Cryo-EM data processing and structure refinement

Data processing was performed using the cryoSPARC v4.7.1 software package[10]. The dose-fractionated movies were aligned by Patch motion correction, and the contrast transfer function (CTF) parameters were approximated using Patch-based CTF estimation with the default settings. Particles were automatically picked using Filament Tracer or pre-trained Topaz[11]. The picked particles were curated by 2D classification.

For the NP6 dataset, a selected class containing 826,701 particles after 2D classification was subject into Non-uniform refinement[12], followed by global and local refinement and reference based motion correction. To deal with the structural heterogeneity of MDA5 filament and scFv NP6, no-align 3D classification was performed using a mask covering the central monomer of MDA5ΔN:NP6: dsRNA duplex. The best class contained 415,377 particles and the resulting 3D map was subjected to Local Refinement, yielding a map with a global resolution of 2.49 Å resolution.

For the filamentous NP6:MDA5:RNA complex, the particle set after 2D classification was further curated by Heterogeneous Refinement using the density of mouse MDA5:dsRNA filament (EMDB 11937) as a reference model. The best class containing 293,099 particles was subjected to Helical Refinement by applying helical symmetry with 76.3 degree twist and 43.5 Å rise, yielding a map at 2.96 Å resolution.

For the F01 dataset, selected classes after 2D classification were curated by ab initio reconstruction with four classes. The best class was subjected to non-uniform refinement[12], followed by local refinement and 3D classification. The class showing clear density for F01 was selected and subjected to CTF refinement, reference-based motion correction, and local refinement, yielding a map at 3.20 Å resolution.

For NP8, selected classes were curated by heterogeneous refinement with six classes. Classes showing the MDA5:RNA filament structure were subjected to non-uniform refinement. A mask was generated for the central MDA5 dimer, and the particles were classified into 10 classes using 3D classification. The best class, containing 257,613 particles was refined using local refinement, yielding a map at 3.07 Å.

For F12, selected classes were curated by ab initio reconstruction and heterogeneous refinement. A mask was generated for the central MDA5 dimer, and the particles were classified into 10 classes. The best class, containing 25,448 particles, was refined using local refinement, yielding an improved map at 3.67 Å.

Model building and validation

Initial models were automatically built with ModelAngelo[13]. The manual model building was performed using COOT[14], with the aid of a density map calculated by DeepEMhancer[15]. Models were refined using real-space refinement in PHENIX[16], and validated using MolProbity[17] from the PHENIX package. The cryo-EM density maps were calculated, and molecular graphics figures were prepared using UCSF ChimeraX[18].

RT-qPCR

For evaluation of type I IFN-β signaling, THP-1 cells were first differentiated into macrophage-like cells[19] by seeding at a density of 0.5 x 10^6/mL in Phorbol 12-Myristate 13-Acetate (PMA, Sigma Aldrich) 62.5 ng/mL. After 24 h, cells were washed with PBS once and rested in complete media for 24 h. Afterwards, cells were seeded into LPS (1 µg/mL) and IFN-γ (20 ng/mL) for 24 h, followed by stimulation with ICs. ICs were formed by incubating 1.8 µM MDA5 protein with 0.06 µM 512 bp dsRNA in binding buffer (20 mM HEPES pH 7.5, 150 mM NaCl, 1.5 mM $MgCl_2$) at RT for 15 min. 1.8 µM antibodies [anti-MDA5 antibodies or human IgG1 lambda isotype control (SouthernBiotech, 0151L-14)] were added and incubated at RT for an additional 5 min. The complexes were stored on ice until they were added directly to culture media for a final concentration of 90 nM MDA5, 3 nM dsRNA, and/or 90 nM mAbs, unless stated otherwise. At indicated timepoints, total RNAs were extracted using TRIzol reagent and cDNA was synthesized using High-Capacity cDNA reverse transcription kit according to the manufacturer's instruction. Real-time PCR was performed using a set of gene-specific primers or random primers, a SYBR Green Master Mix, and the StepOne Real-Time PCR Systems (Applied Biosystems). Primers included: IFNB1 forward 5'-AAACTCATGAGCAGTCTGCA-3', IFNB1 reverse 5'-AGGAGATCTTCAGTTTCGGAGG-3', human ACTB forward 5'-GCACAGAGCCTCGCCTT-3', human ACTB reverse 5'-GTTGTCGACAGCG-3'.

Cellular FcγR blockade assays

After differentiating THP-1 cells into macrophages and seeding into a 24-well plate, cells were incubated with 10 μg/mL of Fcγ receptor antibodies [Fc Block (BD, 564219), CD64 (Biorad, MCA756G), CD32A (BioXCell, BE00224), CD32B (Cell Signaling, 20312), CD32C (MyBioSource, MBS820241), CD16A (Proteintech, 98293-1-RR), or CD16B (Proteintech, 98192-1-RR)] for 1.5 h. Then cells were stimulated with ICs added directly to the media for 4 hours, followed by harvesting cells for RNA.

Immunoblotting

Cells were seeded at 80% confluency in 24- or 48-well plates and stimulated with ICs as described previously. At indicated timepoints, cells were lysed with 1% SDS lysis buffer (1% SDS, 10 mM Tris pH 7.5, 150 mM NaCl, 10 mM DTT), then boiled for 10 min. Supernatant was collected and spun down at 500 *g* for 5 min, and collected in 1x SDS sample buffer (62.5 mM Tris-HCl pH 6.8, 10% glycerol, 2% SDS, 2.5% β-mercaptoethanol), followed by boiling for 10 min. The following antibodies were used for Western blotting: MAVS (Bethyl, A300-782A), TRIF (Cell Signaling, 16809), MDA5 (NP6, in-house antibody), actin (Cell Signaling, 4967).

siRNA electroporation

To knock down transcripts encoding MAVS and TRIF, THP-1 cells were differentiated using PMA 62.5 ng/mL for 24 hours, then electroporated with siRNAs using Neon NxT electroporation system (Thermo Fischer Scientific) according to manufacturer's instructions. siGENOME SMARTPool siRNAs for *MAVS* and *TICAM1* (Horizon Discovery) were electroporated into cells. Cells were recovered for 24 h before polarized with LPS (1 μg/mL) and IFN-γ (20 ng/mL) for 24 h prior to IC stimulation.

ASC foci immunofluorescence imaging

Differentiated THP-1 cells were seeded on coverslips and stimulated with ICs as indicated. Cells were fixed with 4% paraformaldehyde at RT for 10 min and permeabilized with 0.1% Triton-X at RT for 10 min. Cells were blocked for 1 h at RT with 1% BSA in PBS-T, and stained using ASC (1:100, Adiopogen AL177) overnight. After washing with PBS-T three times, coverslips were incubated with secondary antibody for 1 h. Hoechst 33342 (1:3,000) was used to stain the nuclei. Coverslips were mounted using Fluoromount-G and imaged with a Nikon Ti2 motorized inverted microscope with 60x oil-immersion lens and Hamamatsu Flash4.0 LT camera at the Core for Imaging Technology & Education at Harvard Medical School. Images were taken from 12 fields of view from z-stack images (0.11 μm step size). All images were processed and analyzed with Fiji.

In vitro neutrophil extracellular trap (NET) formation assay

Neutrophils were seeded at a density of 0.5 x 10^5 cells per well in HEPES-buffered, phenol red-free RPMI 1640 medium in poly-L-Lysine coated chambered coverslips (μ-Slide 18 Well-Glass Bottom, Ibidi). Cells were allowed to adhere for 30 minutes at 37°C and 5% CO_2. Following adherence, neutrophils were stimulated with either vehicle control, 4 μM ionomycin (Invivogen), or 100nM PMA (Invivogen) for 4 hours at 37°C and 5% CO_2. After stimulation, cells were fixed with 4% paraformaldehyde in PBS for 10 minutes at RT, followed by three washes with PBS.

For immunofluorescence staining, fixed cells were permeabilized with 0.1% Triton X-100 in PBS for 10 minutes and subsequently blocked with 3% BSA in PBS containing 0.5% Tween-20 for 1 h at RT. Primary antibodies against myeloperoxidase (MPO; R&D Systems, AF3667, 1:200) and citrullinated histone H3 (H3Cit; Abcam, ab281584, 1:500) were applied and incubated overnight at 4°C. Following primary antibody incubation, cells were washed three times with PBS and incubated with fluorophore-conjugated secondary antibodies (Abcam, 1:2000) for 2 h at RT in the dark. Nuclear DNA was counterstained with Hoechst 33342 (1:10,000) for 20 minutes at RT. After final washes with PBS, samples were stored in PBS at 4°C prior to imaging. Fluorescence microscopy was performed using a Keyence BZ-X800 all-in-one fluorescence microscope with a 20X objective. Images were acquired from two randomized, non-overlapping fields of view per well. For NETosis analysis, cells were counted based on Hoechst staining, and NETs were considered extracellular DNA strands or smears that can co-localize with MPO or H3cit. H3cit-positive NETs were counted only if they overlaid with Hoechst staining.

Plasma and PBMC RNA-seq library preparation

Cell-free RNAs (cfRNAs) were extracted from plasma using the Plasma/Serum RNA Purification kit (Norgen). To account for fluctuations in RNA isolation and variable RNA content across different patient samples, 4 μl of ERCC (at 1:10,000 dilution, Invitrogen) was added to 2 mL plasma prior to RNA isolation. Total RNA was extracted from human PBMCs using RNeasy mini kit (Qiagen). 4 ul of ERCC (at 1:10,000) was added to 20 ng of PBMC RNA. The concentration of extracted RNAs was assessed using the Qubit RNA assay (Life Technologies) and High Sensitivity RNA ScreenTape (Agilent Technologies). For both plasma- and PBMC-derived RNAs mixed with ERCC, 2 ng of input was used for cDNA library preparation using the SMARTer Stranded Total RNA-Seq Kit v3-Pico Input Mammalian according to the manufacturer's instructions. The cDNA library was sequenced using the Illumina partial lane NovaSeq platform.

RNA-seq analysis

Mapping and differential gene expression analysis. Pair-ended reads were trimmed by Trimmomatic v0.39[20], and mapped to Grch38.p14 by STAR aligner v2.7.9a[21] in splice-aware mode. Resultant bam files were sorted with Samtools v1.21[22] by read coordinates. Sorted bam files were processed by Rsubread[23], and reads were counted for human gene transcripts by Gencode v43 (based on CDR and UTR counts)[24]. Multi-mapping reads were counted by fraction. Read count files were processed in Deseq2[25], and Volcano plots were generated by EnhancedVolcano v1.20.0 with p-values and Log2FC values from Deseq2. For pathway analysis, genes were selected based on indicated criteria (see figure legends) and analyzed using EnrichR[26] with Reactome 2024 database[27]. The -log10 of pathway FDR values were used for ranking and plotting pathway enrichment graphs. For patient-derived plasma and PBMC RNA-seq, ERCC spike-in control was used for normalization. ERCC was mapped to Invitrogen ERCC92 reference, and gene expression and area under the curve (AuC) values were normalized by a loess function[28].

To generate differential gene expression heatmaps for THP-1 cells, sample stimulated with MDA5 filament ICs (with either NP6 or NP8) were combined as one group, and mock groups were used as controls for Deseq2 inputs. Genes with p-adj<0.5 and Log2FC>0 were selected as inputs for Reactome pathways. Genes identified by top Reactome pathways were separated into 3 groups: Cell death/necrosis pathways (shown in Figure 3a), IFN/ISG pathways, and other immune-related genes (shown in Figure 2b). Z-score heatmaps were calculated by the number of standard deviations above or below the mean value of genes for different groups.

LINE/SINE/ERV analysis. Normalized AuC values of all LINE, SINE and ERV regions in Hg38 by Repbase was calculated for patient and HC samples. For each independent LINE/SINE/ERV region, the AuC value of a given patient and an averaged value of HC1/2 were compared, and only the repeat regions with patient over HC Log2FC < -1 or >1 were considered (to be referred as “differential regions”). The sum of AuC values from all differential regions were calculated for each repeat class, and the overall Log2FC of all samples over the mean of HC were used to generate the heatmap.

For gene feature analysis of LINE RNA in Figure 6a and Extended Data Figure 10a, only uniquely mappable reads (MAPQ>10) were used by filtering Bam files. Each read uniquely mappable to a LINE locus was assigned to one of the 7 groups (CDR, 5’UTR, 3’UTR, intron, <3kb upstream, <3kb downstream, intergenic). To account for the LINE orientation relative to genes, each LINE region within 3kb of genes was further divided into “sense potential” or “antisense potential”, and were separately counted in gene feature analysis.

For scatter plots of LINE RNA in Figure 6b and related figures, mean normalized read counts of each LINE region was calculated for each patient or HC1/2 combined. As with above, only uniquely mappable reads (MAPQ>10) were analyzed. LINE regions within 3kb of a gene were labelled as gene-associated LINEs, and further sub-grouped by whether the associated gene is up-regulated, down-regulated or without change in patients over HC TPM value, with a cutoff of Log2FC>0.3, Log2FC<-0.3, and |Log2FC|<=0.3. The top 100 up-regulated genes associated with the most abundant LINE RNA were used as inputs for Reactome pathway discovery by EnrichR.

Quantification of A-to-I editing. Bam files were filtered for MAPQ>10 for unique mapping. Reads containing mismatches relative to Hg38 were selected using bcftools and filtered for regions within Repbase-annotated LINEs. The number of uniquely mapped reads with A-to-G mismatches and other types of mismatches were then counted and normalized to per-million total primarily mappable reads by sample. To eliminate the reads containing true genomic single-nucleotide polymorphisms, mismatches that are consistently present in all reads were eliminated from the analysis.

Analysis of LINE by mapping to Repbase data. We first compared LINE sequences among family members in Extended Data Figure 9d. The Repbase consensus of all L1 repeats were multiple aligned by MAFFT algorithm[29] and sorted by percentage identity values to L1HS. The sorted L1 sequences were used to generate a similarity matrix heatmap by percentage identity values. To analyze sense and antisense LINE transcripts categorized into individual LINE subfamily in Figure 5d, reads were mapped to Repbase in a strand-specific manner and counted and normalized against ERCC. ***Virome analysis***. A virome reference was generated from all curated RefSeq viral genomes (n = 18,670; February 2025). Reads were first mapped to the human genome (GRCh38), and unmapped reads were re-mapped to the virome reference with multi-mapping allowed. Mapping read counts did not support enhanced viral presence in anti-MDA5-DM patients over HC1/2. Different mappers (star/v2.7.9a and bowtie2/v2.5.4) were also tested for this process with similar conclusions.

Data availability

The atomic coordinates have been deposited in the Protein Data Bank with accession codes PDB: 21SJ and 22HM. The cryo-EM maps included in this study have been deposited in the Electron Microscopy Data Bank under the accession codes EMD-67964, EMD-68271, EMD-68272 and EMD68273. The raw sequencing and read count data were deposited in GSE315387. The scripts used in this manuscript were documented in this Github link: (https://github.com/DylannnWX/Mda5_dermatomyositis_manuscript)

References for Methods

1. Peisley, A. *et al.* Cooperative assembly and dynamic disassembly of MDA5 filaments for viral dsRNA recognition. *Proc. Natl. Acad. Sci.* **108**, 21010–21015 (2011).
2. Concha, J. S. S., Tarazi, M., Kushner, C. J., Gaffney, R. G. & Werth, V. P. The diagnosis and classification of amyopathic dermatomyositis: a historical review and assessment of existing criteria. *Br. J. Dermatol.* **180**, 1001–1008 (2019).
3. Van Gompel, E. *et al.* Anti-MDA5 monoclonal antibodies from patients with dermatomyositis - B cell characteristics and differential targeting of the helicase domains. Preprint at https://doi.org/10.64898/2025.12.01.691530 (2025).
4. Lundberg, I. E. *et al.* 2017 European League Against Rheumatism/American College of Rheumatology classification criteria for adult and juvenile idiopathic inflammatory myopathies and their major subgroups. *Ann. Rheum. Dis.* **76**, 1955–1964 (2017).
5. Brinkmann, V., Laube, B., Abu Abed, U., Goosmann, C. & Zychlinsky, A. Neutrophil extracellular traps: how to generate and visualize them. *J. Vis. Exp. JoVE* 1724 (2010) doi:10.3791/1724.
6. Yoshimoto, N. *et al.* An automated system for high-throughput single cell-based breeding. *Sci. Rep.* **3**, 1191 (2013).
7. Meyer, L. *et al.* A simplified workflow for monoclonal antibody sequencing. *PloS One* **14**, e0218717 (2019).
8. Kurosawa, N., Yoshioka, M., Fujimoto, R., Yamagishi, F. & Isobe, M. Rapid production of antigen-specific monoclonal antibodies from a variety of animals. *BMC Biol.* **10**, 80 (2012).
9. Ohi, M., Li, Y., Cheng, Y. & Walz, T. Negative Staining and Image Classification - Powerful Tools in Modern Electron Microscopy. *Biol. Proced. Online* **6**, 23–34 (2004).

10. Punjani, A., Rubinstein, J. L., Fleet, D. J. & Brubaker, M. A. cryoSPARC: algorithms for rapid unsupervised cryo-EM structure determination. *Nat. Methods* **14**, 290–296 (2017).
11. Bepler, T. *et al.* Positive-unlabeled convolutional neural networks for particle picking in cryo-electron micrographs. *Nat. Methods* **16**, 1153–1160 (2019).
12. Punjani, A., Zhang, H. & Fleet, D. J. Non-uniform refinement: adaptive regularization improves single-particle cryo-EM reconstruction. *Nat. Methods* **17**, 1214–1221 (2020).
13. Jamali, K. *et al.* Automated model building and protein identification in cryo-EM maps. *Nature* **628**, 450–457 (2024).
14. Emsley, P., Lohkamp, B., Scott, W. G. & Cowtan, K. Features and development of Coot. *Acta Crystallogr. D Biol. Crystallogr.* **66**, 486–501 (2010).
15. Sanchez-Garcia, R. *et al.* DeepEMhancer: a deep learning solution for cryo-EM volume post-processing. *Commun. Biol.* **4**, 874 (2021).
16. Liebschner, D. *et al.* Macromolecular structure determination using X-rays, neutrons and electrons: recent developments in *Phenix*. *Acta Crystallogr. Sect. Struct. Biol.* **75**, 861–877 (2019).
17. Williams, C. J. *et al.* MolProbity: More and better reference data for improved all-atom structure validation. *Protein Sci. Publ. Protein Soc.* **27**, 293–315 (2018).
18. Pettersen, E. F. *et al.* UCSF ChimeraX: Structure visualization for researchers, educators, and developers. *Protein Sci. Publ. Protein Soc.* **30**, 70–82 (2021).
19. Genin, M., Clement, F., Fattaccioli, A., Raes, M. & Michiels, C. M1 and M2 macrophages derived from THP-1 cells differentially modulate the response of cancer cells to etoposide. *BMC Cancer* **15**, 577 (2015).
20. Bolger, A. M., Lohse, M. & Usadel, B. Trimmomatic: a flexible trimmer for Illumina sequence data. *Bioinformatics* **30**, 2114–2120 (2014).
21. Dobin, A. *et al.* STAR: ultrafast universal RNA-seq aligner. *Bioinformatics* **29**, 15–21 (2013).
22. Li, H. *et al.* The Sequence Alignment/Map format and SAMtools. *Bioinformatics* **25**, 2078–2079 (2009).
23. Liao, Y., Smyth, G. K. & Shi, W. The R package Rsubread is easier, faster, cheaper and better for alignment and quantification of RNA sequencing reads. *Nucleic Acids Res.* **47**, e47 (2019).
24. Mudge, J. M. *et al.* GENCODE 2025: reference gene annotation for human and mouse. *Nucleic Acids Res.* **53**, D966–D975 (2025).
25. Love, M. I., Huber, W. & Anders, S. Moderated estimation of fold change and dispersion for RNA-seq data with DESeq2. *Genome Biol.* **15**, 550 (2014).
26. Xie, Z. *et al.* Gene Set Knowledge Discovery with Enrichr. *Curr. Protoc.* **1**, e90 (2021).
27. Milacic, M. *et al.* The Reactome Pathway Knowledgebase 2024. *Nucleic Acids Res.* **52**, D672–D678 (2024).
28. Bao, W., Kojima, K. K. & Kohany, O. Repbase Update, a database of repetitive elements in eukaryotic genomes. *Mob. DNA* **6**, 11 (2015).
29. Katoh, K. & Standley, D. M. MAFFT Multiple Sequence Alignment Software Version 7: Improvements in Performance and Usability. *Mol. Biol. Evol.* **30**, 772–780 (2013).